Electrostatic model for antenna signal generation from dust impacts. Numerical simulations and laboratory experiments.

Supervisor: Mauro Massari
Co-supervisor: Zoltan Sternovsky

Graduating student:
Alessandro Garzelli, identification number 918386

Academic year 2021-2022

The present work is dedicated to:

- *My dad, aunt Pina and all those people who raised me as their own child even if I was not. Your unconditioned trust has been my arc reactor until today.*
- *My mum, uncle Johnny and my brother because you have been my support every time I needed it. I owe who I am to you.*
- *James Pyle and his wonderful family for the constant support , food and night drinks in their motorhome. James, hadn't it been for you, I would have quit years ago. Thank you my friend.*
- *Jay Funderburke for his instant friendship and sustain.*
- *Cliff Ruggles for his friendship and the time found in his busy schedule to have lunch with me and James.*
- *My long time brothers Rocco and Francesco. We are always going to be bonded by a strong and unbreakable link no matter where we are going to live in the future.*
- *To Domenico, Viviana and Alessandro for their friendship. I know that you will become great parents one day.*
- *Bowie and Imma. I am very sorry I won't be present at your wedding. I won't be able to see Imma starting to ruin Bowie's life. What a shame. Bowie, in case you want to escape, you can always come with me. I love you Scumbag.*
- *My ladies Susanna, Ylenia, Anna Giulia, Chloé and their newly arrived kids. You have become part of my family and I will be waiting for you to continue the tradition that I started with Susanna. Bus parties.*
- *Sabatino e Matteo and their families for the help and sustain I received while I was in Rome. I will be waiting for you to make more trips and eat Sabatino's rotten food before the trip.*
- *Domenicone and Cinzia for the best lunch I had in Rome in five years. I am still waiting to meet Cinzia's Russian friends.*
- *Gabriele and Staccino for being the best roommates ever. I never had younger brothers but I bet that what we have is a similar bond.*
- *to Domenico, Nickname Verzell, his Brother Donato, Mario and Anna for being my first neighbors.*
- *to Roberto, Pino, Raffaello, Enrico, Andrea and to our effort to unmask the only real avenger that walks around us. His powers are limitless but we will stand still.*

Abstract

Transient voltage perturbations are caused by dust impacts on spacecrafts and captured by the Radio Plasma Wave Science instruments. The plasma cloud generated after the impact is responsible for the generation of the waveforms by means of the interaction between the antennas and spacecraft main body. This thesis presents a general electrostatic model that takes into account the collection of the charge of the spacecraft and the flight of electrons and ions to infinity. The escape, carried out by positive and negative carriers, is characterized by an enormous difference in speed and causes the typical shape of the waveforms. Numerical simulations are performed to reproduce the signals generated by the RPWS mounted on the spacecraft considering as a discriminating parameter the impact location. The spacecraft-antennas mutual interaction is described using the Maxwell capacitance matrix. A spherically shaped spacecraft equipped with four cylindrical antennas is fabricated in order to conduct experimental impact measurements with the dust accelerator facility. The antennas are configured as two monopoles and a dipole. Dust particles, accelerated at velocities greater than 20 km/s, impact the satellite and the consequent waveforms captured by the antennas are recorded. The fitting of the data provides good to excellent results using few fitting parameters, such as the ion and electron escape speeds. As a final step, calibration tests of an Hexanode delay line detector were conducted to determine the shape of the expanding ions. The presented general model creates a step by step procedure to analyze waveforms produced by antennas. Missions investigating the distribution of dust particles in different space environments are many and the presented electrostatic model can be applied to study the generated space dust waveforms.

Acknowledgement

Contents

List of Figures

List of Tables

Chapter 1

Introduction

Cosmic Dust , also referred as space dust, is composed of fine particles of solid matter. In can be distinguished by its astronomical location:

- Intergalactic dust is composed by particles present between galaxies and intergalactic space.
- Interstellar dust present in the interstellar medium, the tenuous gas and dust that fills the void between stellar systems and galaxies.
- Interplanetary dust, or zodiacal cloud, pervade the space between planets within a planetary system like the solar system.
- Circumplanetary dust present in planetary rings.

The typical size of a dust grain range between the dimension of a single molecule to 100μm, larger particles are classified as meteoroids. In the solar system the presence of cosmic dust is revealed by the zodiacal light, or false dawn, which is a faint and diffuse white glow visible in the night sky from Earth. Such phenomenon is caused by the scattering of sun light because of cosmic dust. For many years zodiacal light provided information on properties of dust particles such as spacial distribution, density number, size, shape, structure and material. The measurements were performed using different wavelength of the light spectrum. The Helios zodiacal light experiment mounted a space born zodiacal light photometer that operated at short wavelength, 330-550 nm, instead the Cosmic Background Explorer mounted an infrared camera, 1-300μm. Cosmic dust are found deposited in Greenland, the Antarctic ice or on the oceans floors because they are trapped in the Earth magnetic field. As cosmic dust are ejected from celestial bodies they carry valuable information about their parent bodies such as composition and structure. These information and their incoming trajectories are difficult to retrieve once the particle has experienced the high temperature of the atmospheric reentry. Cosmic dust store more information than just structure and composition of the place of origin, in fact during their journey through deep space they are impacted by their own kind, eroded by the solar wind, charged by photoelectric emission or accreted by extraneous molecules. All these information can be better retrieved by in-situ experiments carried out by modern satellites.

1.1   Dust impact detection

The devices that have been used in the past years to detect and characterize cosmic dust are many. The present work gives a brief description of Cosmic Dust Analyzers in the first chapter to examine the impact ionization phenomenon, and how it is related to space missions and provides a more extensive analysis of antenna dust detection. Im-

pacts between satellites and cosmic dust are a common event in space and they have been observed using electrostatic antennas since the 1980s with the Voyagers spacecraft.
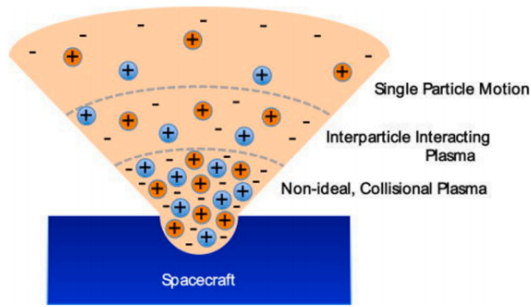
Figure 1.1: simplified example plasma expansion after a dust impact.

Antenna dust detection cannot replace the usage of dedicated dust analyzers on spacecrafts but they are of great importance because all space born missions carry electric equipment on-board making the availability of information very easy. The biggest limitations of electric field antennas is that they cannot provide any information about the chemical composition of the impacting object while dust analyzers are often used in combinations with Time of flight detectors. However, mass measurement can be done on the mass of the impacting objects through the signals captured by the antennas of the spacecraft after the impact. Hypervelocity dust impacts generate a cloud of plasma that expands isotropically with a conical shape. The most accredited model on impact ionization proposed by S. Drapatz and K. W. Michel [3] in 1974, chapter 2, describes the phenomena as follows:

The kinetic energy of the hypervelocity grain is converted into heat at the moment of the impact. A Shock compression wave propagates inside the target material and the grain. Once the wave reaches the free end of the grain an expanding shock is generated and the expansion begins. The grain and part of the target material vaporizes leaving a crater on the impact location. Heat generated after the impact is enough to thermally ionize the vapour creating a gas composed by electrons and ions in atomic or molecular form. At the beginning of the expansion matter is in a high dense state and recombination processes occur, chapter 2. In the later stages of the expansion thermal equilibrium is reached and a residual ionization remains. The residual charge produced after the impact is referred as charge impact and can be empirically computed as $Q = km^{\alpha}v^{\beta}$ where k, α and β are fitting constant parameters obtained thought experimental data that depend on the impacting and target material, angle of impact and chemical composition of the impactor. As mass scale linearly with respect to charge and it is independently from velocity, it is possible compute the mass of the grain if charge and velocity are known. Knowing the mass of the grains impacting the satellite it is possible to obtain a time and space dependent mass distribution of cosmic dust fluxes. S. Drapatz model predicts the presence of solid fragment at lower impact speeds coming from the missed vaporization of the grain or the target. The empirical formula that allows to compute the impact charge is highly uncertain and a brief summary of the results in the literature is present in chapter 2. Such results are obtained performing experiments using electrostatic accelerators like the one present at the Colorado University of Boulder described in detail in chapter 4. The expanding impact charge is detected by the electrostatic field antennas as it perturbs the equilibrium potential of the spacecraft. The floating potential model proposed by Zaslavsky [12] is described in chapter 3. Considering a dust impact occurring on the spacecraft body, the potential of the spacecraft is perturbed from its equilibrium following three steps. The expansion of the plasma cloud in its first stages does not modify the equilibrium potential as plasma is by definition neutral. Electrons are the lighter, therefore faster, particles in the cloud and the initial seconds(μs) of the voltage perturbation is the fastest and caused by electrons expansion, blue curve, Ion escape (red curve) and the final negative relaxation that occurs as $\Phi_{sc} \sim e \exp\{-t/\tau\}$ where τ is the relaxation time that depends on the

Figure 1.2: All the possible charging mechanism of a spacecraft with different environmental condition.

shape of the spacecraft and the space environment. The same mechanism occurs on the antenna at the same time and, with a simple monople antenna configuration, the Radio Plasma Wave Equipment of the spacecraft would read the difference between the antenna potential and the satellite potential. It is worth noticing that the discharge time τ is of fundamental importance to the generation of the waveform. The main goal of this thesis is to create an alternative electrostatic model to the one proposed by Zaslavsky that takes into consideration the work done by Maxwell [1] on system of conductors. The model will be used to fit the voltage curves obtained during a laboratory controlled experiment and the values obtained with the fitting procedure confronted with the literature. As first step of approximation the conical shape of the expanding plasma is going to be considered as it were to be a spherical point charge moving on a straight line. To determine the angular distribution $\Theta = \Theta(v)$, where Θ is the semi-aperture of the expanding cone and v is the impact velocity of the dust, an experiment with a Three-Layer Delay Line Detector is going to be performed, chapter 4.

1.2 Radio Plasma Wave Science

1.2.1 Cassini RPWS
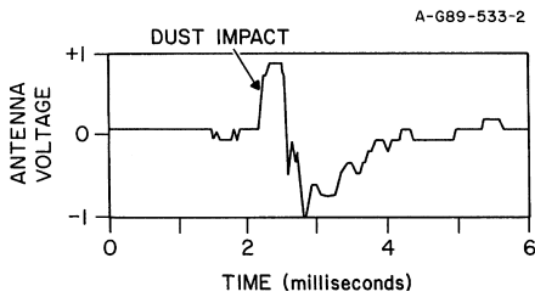
Figure 1.3: Voyager dust impact detected on August 26, 1981

The Cassini radio and plasma wave investigation was designed to study radio emission, plasma wave, Thermal plasma and dust in the vicinity of Saturn. The dust investigation is the proximity of Saturn was prompted as during Voyager 2 flyby of the planet, the plasma wave and radio astronomy instruments detected impacts of microns sized dust on the spacecraft surface. Signals like the one showed in figure 1.3, were detected by Voyager as the spacecraft was crossing Saturn's ring plane at 2.88 R_s. The rate of impact was 0.1/s. With respect to the Voyager spacecraft, Cassini was

3

equipped with better electronics to study dust particles in the Saturnian environment. The most important change was to equip Cassini with a two sets of antenna configurations. A monopole and a dipole antenna. As it will be shown in the next section a monopole antenna is more sensitive to dust impact with respect to a dipole. Signals on Voyager were most of the times saturated due to the 4-bits resolution of the waveforms.

1.2.1.1 Electric antennas

The antenna elements consist of conducting cylinders of length 10 m and diameter 2.86 cm. The elements are made of beryllium-copper, silver plated on the exterior surface and painted black on the interior for thermal control. The surface of each antenna has a 12% perforated area to let sunlight pass through the shaded parts to prevent thermal bending. The physical orientation of the three elements with respect to the x,y and z body axes are the following:

- E_u and E_v have a polar angle θ measured form the z axis of the spacecraft of 107.5°

- E_w has a polar angle of 37°

- The azimuth angle measured with respect the x axis is 24.8°, 155.2° and 90° for E_u, E_v and E_w respectively.

Figure 1.4: Cassini spacecraft antenna orientation with respect to the body frame.

The E_u and E_v antennas lie on the same plane and they form a dipole antenna. E_w extends perpendicularly form the plane formed by E_u and E_v and it forms a monople antenna in combination with the spacecraft body.

1.2.1.2 Wideband Receiver

The wideband receiver served as front end for dust detection on board of Cassini and it was equipped with a data compression processor to search waveforms with similar signature of dust impacts based on those observed with Voyager, fig 1.3. The wideband receiver processed signals coming from a single selected detector E_u, E_v or E_w. The instantaneous dynamic range of the receiver was 48 dB. The dynamic range of the incoming signals was expected to be large and a set of discrete gain amplifiers and an automatic gain control were used to amplify the signal in step of 10 dB over a range of 0-70 dB. The total dynamic range of the system was 100 dB. Two band pass filters follow the series of amplifiers with selecting frequency of 60 Hz to 10. kHz or 0.8-75 kHz. The output of the selected pass band filters was sent to a analog to digital converter that a sampling rate of 27,777 samples/s for the first channel and 222,222 samples/s for the second channel.

1.2.2 STEREO RPWS

Stereo is a NASA mission launched on 26 October 2006 with the aim to study coronal mass ejection. The mission consist of two twin spacecraft orbiting the sun at around 1 AU. STEREO equipment discovered a high time variable flux and its possible cause seems

to be nanometre-scale dust impact on the surface of the two spacecraft.

1.2.2.1 Electric antennas

Both STREREO spacecrafts are equipped
with 6m long Beryllium-Copper stacer el-
ements installed in a magnesium and alu-
minum housing that provides launch stor-
age, deployment means, and support at
the proper orientation. Figure 1.5 shows
predisposition of STEREOS antennas and
their orientation with respct to the space-
craft body. Each spacecraft consists of an
assembly of three antennas mounted to a
single interface plate that is oriented oppo-
site to the sun direction, anti-sun side -X.
When deployed, the three antennas form a
mutual orthogonal pattern, inclined of 35°

Figure 1.5: STEREO antenna configuration

degrees with respect to the spacecraft deck. The three antennas are oriented in such a way
that they form a cube and the vertex of the cube encounters the spacecraft. The angle
that separate each antenna, -X direction, is 120°.

1.2.2.2 Time Sampler Domain

STREREO spacecrafts are not equipped with a dedicated receiver to detect dust impact
like Cassini but its Time Domain Sampler samples waveforms simultaneously from the
three orthogonal antennas. Hence it is capable of three different monople voltage signals
at the same time. Furthermore it is capable of taking a pseudo difference between two
monopoles to obtain a fictitious dipole antenna. The aim of the TDS is making very fast
samples of the time domain while making use of the telemetry downlink. It can produce
time domain sampling at a rate of 16 million bit per second compared with the downlink
rate that is 500 bit per second. The TDS is capable of choosing event with a triggering
system that takes snapshots when sampled amplitudes reach a commandable threshold.
With this system in place it is able to drastically reducing the downlink rate.

1.3 Cassini dust detection
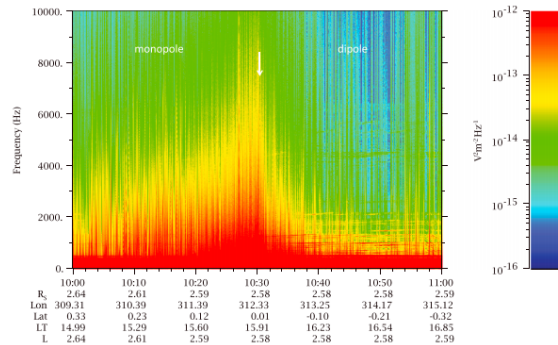
Figure 1.6: Cassini spectral power of the ring plane crossing occurred on DOY 001, 2016 where there was a switch
from monopole to dipole configuration in order to analyze and compare the results

5

The previous dust signal detection performed by Cassini and STEREO were what inspired this entire work. Cassini ring crossing was fundamental to analyze and compare dust detection using monople or dipole configuration. As explained in the section dedicated to Cassini WBR, monople and dipole detection could not be performed at the same time. Figure 1.6 shows a 1 hour period the crossing of Saturn rings plane and the white arrow shows the moment when there was the switch from monople to dipole dust detection. The power at the moment of the switch reduced of 10 dB. The power spectrum of the signals is a function of the dust impact rate and the averaged square of voltage amplitude. The decrease in power could be due to one of the latter factors or both. Figure 1.7 shows the histograms of voltages of a ring crossing event happened on DOY 340, 2015 in monople and dipole mode. Comparing the plot it can be seen that the voltage amplitudes are comparable in the two configurations. Under the assumption that the dust distribution is constant within the rings it is safe to say that dipole antennas detect voltage as monople antennas. The decrease of power showed at the moment of the configuration switching is due to a lower rate of event. A statistical study of the two crossing was performed by Ye at all [14]. Figure 1.8 refers to the ring crossing that happened on the 2016.
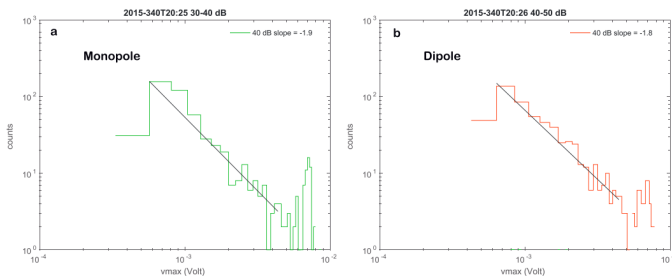
Figure 1.7: Cassini voltage histogram in monopole and dipole configuration of on DOY 301, 2015 showed that the amount of voltage detected by the two configuration is comparable.

The plot shows the impact rate of positive and negative events, the number ration between the two and the ram angles governing the attitude of the satellite as function of time. The blue crosses are the negative events while the red represent the positive ones. In monopole configuration the negative counts are due to dust hitting the spacecraft body, while positive counts are due to antenna hits. After switching from monopole to dipole the count of negative signals drops drastically. Looking at the ratio between the impact rates it is possible to see that it changes from -0.2 to 0.8 indicating that in dipole configuration negative and positive events are comparable in number. The amount of positive and negative events in dipole configuration is comparable to the number of positive event in monople indicating that the impacts in dipole configuration occur on the antennas (E_u for positive and E_v for negative). Figure 1.9 shows the statistical study of the dipole configuration done for the 2015 ring crossing. The plot has a period of two hours and it can be observed that the number of both signal polarities is comparable in a dipole configuration. There is a negative peak at the time of Encelado plume crossing. The ratio positive to negative increases as the satellite changes its attitude as it can be seen by the changing of the ram angles. The change in orientation of the satellite changes the effective areas of the antennas modifying the ratio number. The Cassini ring crossing confirmed that dipole configuration detects a smaller amount of hits because of the lesser active area of the antenna with respect to the monopole configuration and the impact location can modify the polarity of the signal. Dust impact location is the topic dealt in chapter 3 when an experimental set up is going to be readied along with numerical simulations to create an electrostatic model.
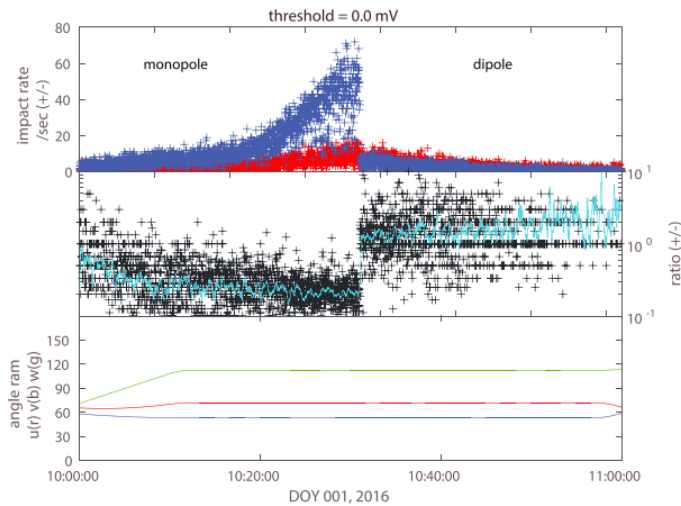
Figure 1.8: Cassini statistical reconstruction of the ring plane crossing occurred on DOY 001, 2016 where there was a switch from monopole to dipole configuration in order to analyze and compare the results
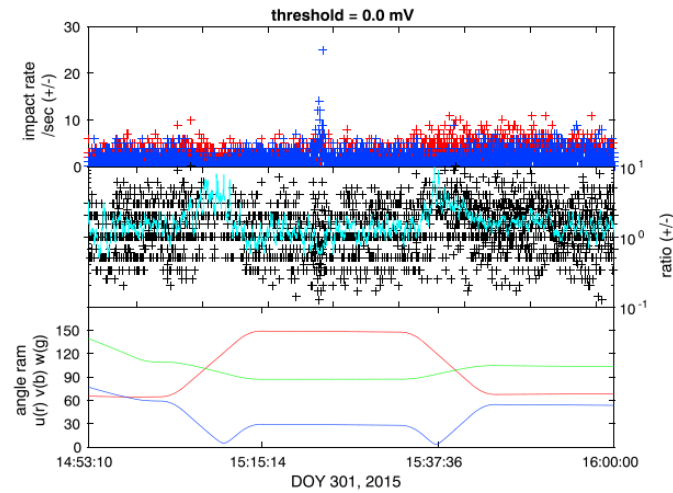
Figure 1.9: Cassini statistical reconstruction of the ring plane crossing occurred on DOY 301, 2015 where the dipole antenna configuration was used.

1.4   STEREO dust detection

STEREO A and B, revealed a flux of sub micrometre dust that is highly variable with time. The RPWS of STEREO is composed of three orthogonal electric filed antennas in monople configuration. The waveforms recorded by STEREO are visible in figure 2 and they can be divided in 6 different shapes. The most common shape is the single hit waveform that was recorded in the 79% of the cases and shows a positive charging of one antenna with the other two antennas being at a nearly zero voltage. The 7% of the single hits are inverted with the overshoot still present. The remaining 20% of the waveforms are generated by impacts on the spacecraft body. The single hit waveform is the most common of the signals captured by STEREO and it does not have a theoretical interpretation yet. The fact that just one antenna is capturing a signal and the others are not means that the hit occurs on the antenna E_x and all the escaping electrons are captured by the antenna and the spacecraft is not collecting any charge. An explanation for the negative overshoot both for the single hit and inverted single hit is still missing. The triple hit has a clear interpretation. The body of the spacecraft is hit by interplanetary and interstellar particles. The rise time of the main signal is of the order of tens of microseconds that

is comparable with the charge collection mechanism. The negative overshoot after the positive spike is due to the different discharging time constant of the three antennas. The E_y signal has a second overshoot after the first negative one making the signal positive again. There is no explanation in the present model for this behaviour. The 6% of the triple hit are inverted in polarity and the most probable explanation for this event is that dust impacts occur in the immediate vicinity of the antenna base where electrons from the impact plasma can be recollect with high efficiency. The other scenario is represented by the unlikely event that the spacecraft collects positive charges despite having a positive potential.

A small subset of event have a negative preshoot before the positive spike and this is due to the fast escaping electrons followed by the expansion of ions. The relaxation time depends on the discharge of each antenna. The triple hit with a negative preshoot is a very rare event that can be explained with a dust impact location on the antennas that refers to the E_x monopole. The very fast preshoot is certainly due to fast escaping electrons. The negative ongoing signal is to be related to negative charge collection of the antenna because the discharge time is significantly longer with respect to the spacecraft discharge time. The positive overshoot is similar to the one of the inverted single hit to which the floating potential model presented in chapter 3 gives no explanation.
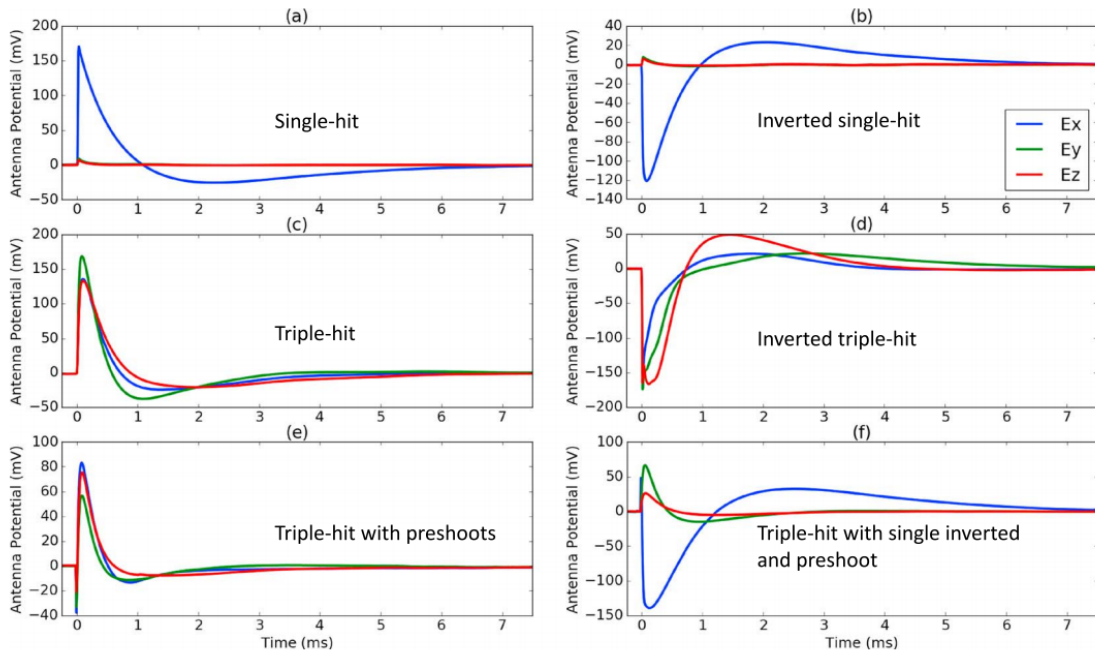
Figure 1.10: Waveforms generated by STEREO monopole antennas.

Chapter 2

Dust Impact ionization

2.1 Shock wave impact ionization of dust particles

Hyper velocity collisions between dust particles and solid surfaces occur very frequently in the planetary system. The result of these collisions is the Ionization of the particle and the target. The ionization process is different depending on the impact velocity of the particle while the different densities of the particle and the target govern the formation of the crater on the impinged target. If the density of the particle is order of magnitudes lower with respect to the target the strength of the shock-wave generated after the impact inside the particle and the target will depend on the normal component of the impacting velocity. In case in which the density of the target is higher but comparable with the density of the particle or the density of the particle is order of magnitude higher than the density of the target the subsequent shock-wave's strength depends on both the normal and perpendicular components of the impact velocity. The dust impact velocity has a fundamental role in understanding the processes behind the ionization and there is a distinction between Low and High Impact Velocity.

After the impact the gas dynamic that follows is determined by the conversion of the kinetic energy into heat. A shock wave start propagating inside the particle and the target. While the shock wave in the target fades away traveling at a certain distance, the one inside the dust reaches the other side of the free material. The shocked state of the material is obtained applying the equations of the conservation of mass, momentum and energy of a 1D wave. This process can be done in a reference frame on the traveling wave, case c, or in a fixed frame, case d. If the frame system is moving with the shock-wave, its velocity is zero and U_1 and U_2 are the velocity of the undisturbed and shocked material respectively. If the frame system is fixed than the velocity of the shock-wave is U_s, U_p is
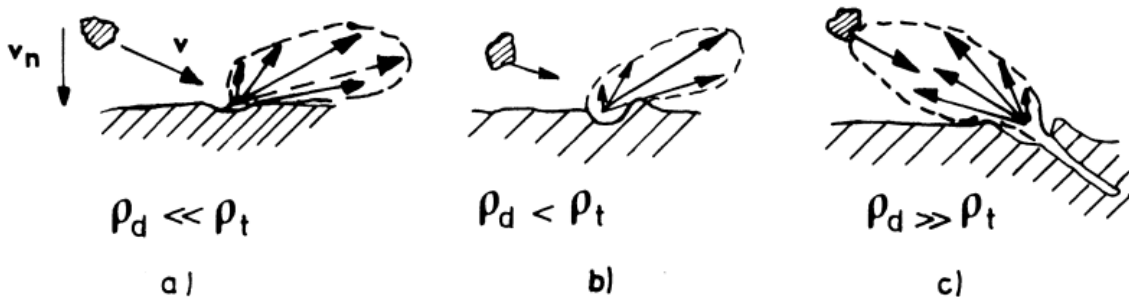
Figure 2.1: The density ratio between the target and the particle.
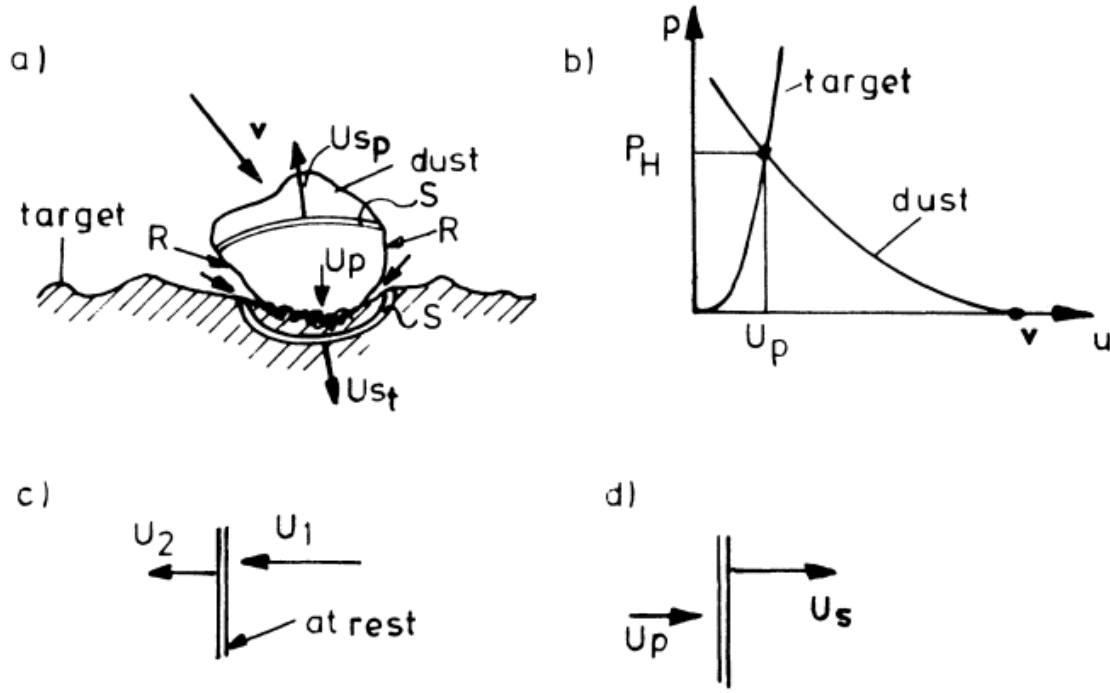
Figure 2.2: Sketch of a dust impact on a solid surface. In the b picture there is a simple example of a Hugoniot-curve to find the shocked state behind the strong shock

the velocity of the material behind the shock and the velocity of the undisturbed material is 0. At the moment of the impact the velocity behind the shock U_p is the same for the target and the particle. The particle slows down from a velocity v to U_p while the target is accelerated from a resting condition to U_p. Case b, in Figure 2.2, is the Hugoniot-curve for the particle and the target and the intersection of the two curves gives the pressure of the shocked state. Case a, in Figure 2.2, is the sketch of the particle impacting with velocity v on the target and the shock-waves propagating in opposite directions. R is the rarefaction-wave propagating backwards inside the material once the shock-wave reaches the end of its path. The rarefaction-wave transforms heat into expansion energy and the material expands into vacuum. The energy transformed into expansion energy is the energy behind the shock E_H and it is divided into three component ΔE_{el}, elastic energy, ΔE_i, energy of the nucleus of the atoms, and ΔE_e, energy of the excited electrons. The delta in front of the energies states the variation that the energies undergo from the stationary state. Figure 2.3 is the plot of ΔE_H for a $1\mu m$ iron particle impacting on a tungsten target. It can be seen that at lower velocities the elastic energy is predominant and electrons do not have enough energy for evaporation to take place. When impact velocities reach 20 km/s, or higher values, electrons thermal energy is the highest one and the particle evaporates completely. The variation of energy shown in the plot can be approximated by the energy equation for strong shocks, Eq. 2.1, for impact velocities higher than 10 km/s. It is possible to notice how the change in energy is due to the kinetick energy of the material behind the shock and it increase with the second power of the impact velocity multiplied by a constant that depends on the initial densities of the particle and target material. Eq. 2.1 can be used for any kind of impact and target material.

$$\Delta E_H = \frac{1}{2}u^2 = \frac{1}{2}\left(\frac{w}{\sqrt{\frac{\rho_{fe}}{\rho_w}}+1}\right)^2 \tag{2.1}$$

10
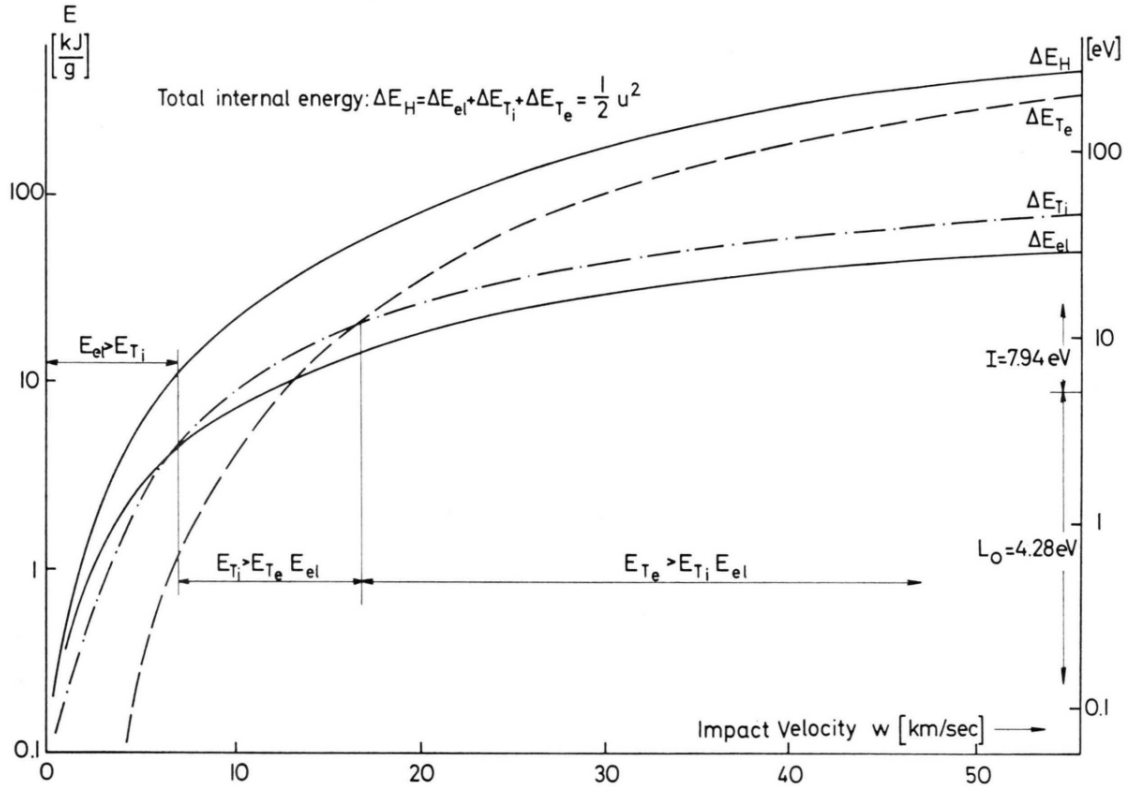
Figure 2.3: The different contributions to the total energy ΔE_H behind a shock wave through Fe upon impact onto W at velocity w: elastic energy ΔE_{el} e thermal energy of nuclei ΔT_i and of electrons ΔT_e

2.1.1   Low velocity impact

In this kind of impact elastic energy is predominant and the variation of kinetic energy of the electrons is not high enough to vaporize the entire particle. For an iron particle hitting a tungsten target with a velocity of 6 km/s just the 5% of Fe is to be found in vapour form and the remaining 95% is liquid.

$$< x >= \sqrt{2D(T)\tau} \tag{2.2}$$

where D is called diffusion coefficient, measured in squared meters per second and must be determined experimentally each time depending on the materials of the particle and the target, and τ is the cooling time and represents the time during which the impurities can evaporate in the liquid on the surface. The portion of the evaporated impacting particle can be computed using the well known Hertz-Knudsen equation

$$\frac{\Delta M}{\tau} = 4\pi r^2 P \sqrt{\frac{m}{2\pi kT}} \tag{2.3}$$

where on the right hand side the area on the surface on which the evaporation takes place is considered to be circular and the radius r must be determined experimentally, P is the pressure of the material evaporating which can be found in tables, m is the mass of the particle hitting the target, k the Boltzmann constant and T is the temperature. The degree of the Ionization of the evaporated material can be computed using Saha-Langmuir equation

$$\frac{n_i}{n_0} = \frac{g_i}{g_0} \exp\left(\frac{e(\Phi - I)}{kT}\right) \tag{2.4}$$

where g_i and g_0 are the statistical weights of ions and atoms, Φ and I are the work function and ionization potential of the evaporating material.

11

2.1.2 High velocity impact

High impact velocities cause the pressure behind the shock to reach values 5 times higher with respect to the initial one and the state of the matter can be computed using the strong shock equations

$$\frac{V}{V_0} = \frac{\rho_1}{\rho_2} = \frac{(U_s - u_p)}{U_s}$$

$$p_H = p_2 = \rho_1 U_s u_p + p_1 \qquad (2.5)$$

$$e_H = e_2 = \frac{1}{2}(p_1 + p_2)(\frac{1}{\rho_1} - \frac{1}{\rho_2}) + e_1$$

Equations 2.5 are referring to a fixed frame where the subscript 1 and 2 refer to the conditions of the matter in front of and behind the shock. The compression ratio V/V_0 HVI is circa 1/5 and the high densities and pressures cause the electrons in the nucleus to crushed into a smaller volume and energy bands tend to become broader. In this complicate scenario the Thomas-Fermi model gives a statistical description of situation where a Z-folded atom is surrounded by a continuous cloud of electrons. The whole system is contained into a sphere with a radius $R_0 = (\frac{3}{4\pi n})^{\frac{1}{3}}$, where n is the electron density. The compression caused by the shock-wave and the subsequent expansion due to the relaxation wave is described in figure 2.4. The electron cloud volume is brought from its initial state described by density and temperature to the high pressurized state by the shock wave. At this point it is assumed that the particle is completely vaporized and the expansion begins assuming a local thermal equilibrium condition. The expansion is considered to be fast and Isentropic

$$\frac{p\delta V + \delta E}{T} = \delta S = 0 \qquad (2.6)$$

The LTE condition holds until a lower density is reached and the ionization process
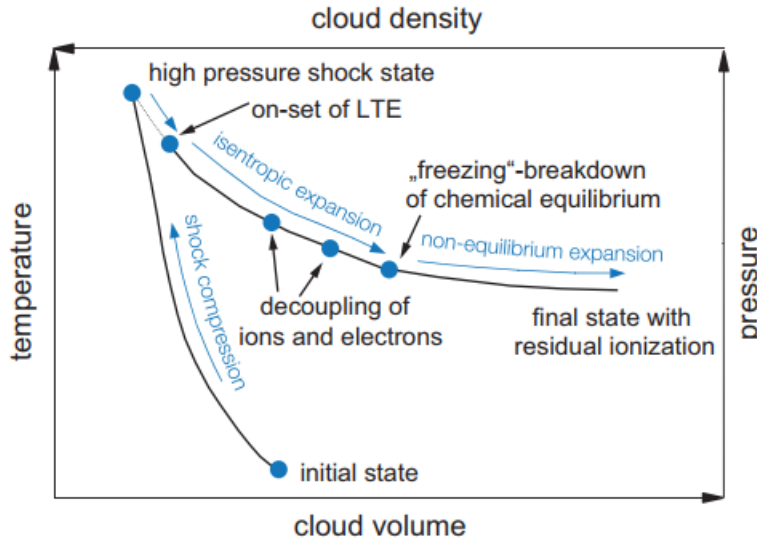
Figure 2.4: The phases of the shock wave ionization expasion as explained in the Drapatz model in 1979

is determined as a recombination process in an ideal gas. This passage is considered instantaneous and the and the entropy for the high pressurized state

$$S = \int_0^{T_s} C_v \, d\log T \qquad (2.7)$$

must be equal to the entropy at lower densities

$$S = (1 - i)S_N + i(S_+ - S_e) \qquad (2.8)$$

where the entropy of neutrals, ions and electrons have been considered. i is the ionization degree and it can be computed using Saha-Equation

$$\frac{i^2}{1-i}n = 2\frac{g^+}{g}\frac{(2\pi m_e kT)^{\frac{3}{2}}}{h^3}\exp\left\{-\frac{I_0 - \Delta I}{kT}\right\} \tag{2.9}$$

where, n is the cloud density, g^+ and g are the statistical weight of ions and neutrals, k is the Boltzmann constant, h is the Plank constant and ΔI is the lowering of the ionization limit. From the point where the LTE is lost the gas expands to infinity with state of residual ionization that reaches an asymptotic value. The residual ionization is a function of the impact velocity and the size of the impacting particle. The plot in figure 2.5 shows the residual ionization of two different iron particles on a tungsten target. The residual plot has a lower limit because for lower velocities the residual ionization is a surface ionization and the model low velocity impacts must be used. Furthermore the residual ionization does not depend on the mass of the hitting particle for velocities higher than 45 km/s.
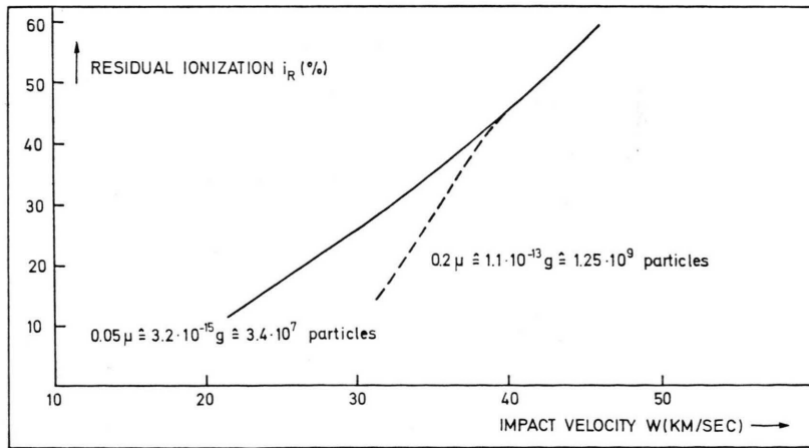
Figure 2.5: The residual ionization of the expanding impact material as function of the impact velocity and mass

2.2   Charge Yield

The residual Ions have a net positive charge expanding into vacuum and the positive charge is neutralized by electrons making the material leaving the target plasma. The cloud produced after the impact has an equal number of positive and negative carriers

$$Q^- \approx Q^+ = Q \tag{2.10}$$

The total charge Q generated depends on the first impact between the target and the incoming particle, which is called primary impact, and the subsequent impacts caused by the ions generated by the primary impact and the surroundings. The latter is called secondary impacts and the charge generated depends on the impact velocity of the primary impact and the geometry of the surrounding near the location where the first impact occurred. The dust analyzer mounted on Cassini, shown in Figure 2.6, was able to detect the charge of the particle entering the detector with two inclined grounded grids, Q_p, the positive and negative charge produced after the impact. The charged particle entering the cosmic dust analyzer hits the target, chemical analyzer target, which is biased with 1 kV to separate electrons and ions. Electrons are collected by the target which generate the signal Q_C and ions are pushed towards the ion collector that generates the signal Q_I. Ions generated after the first impact have an angular and velocity distribution that depend
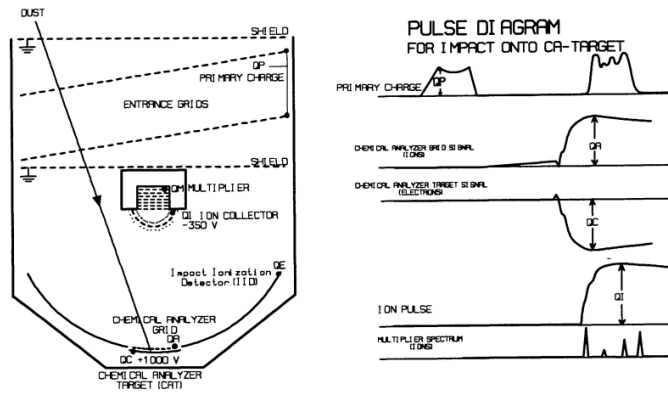
Figure 2.6: Cassini Cosmic Dust Analyzer with his hemispherical target and Ion collector.

on the velocity of the the first impact and the angle between the velocity vector and the normal to the surface of impact. Some of the Ions are suddenly attracted by the negative voltage of the the ion detector, while others hit the grid in front of the target,Q_A, or the impact ionization detector generating a second cascade of ions. This event continuously repeats itself until all ions are collected. The charge generated by the first impact causes the first steep ramp in the signals while the charge generated by the secondary impacts is responsible for the the second slower ramp.The total rising is a function of the impact velocity and does not depend on the mass of the particle. The plot of impact velocity and rising time can be seen in Figure 2.7 for the HEOS 2 sensor. The time for the signal to reach its peak is lower at higher velocity and the curve is less steep at low velocities. The mass of the particle is obtained using the following equation

$$Q = Km^\alpha v^\beta \tag{2.11}$$

where Q is the impact charge, m is the mass of the particle hitting the target and v is its velocity. K α and β are constants that are determined experimentally. The charge yield Q generated has a proportional dependence on the mass of the particle m. Figure 2.7 shows the results of an experiment conducted at the Max-Plank institute by H. Dietzel at all. [2] where iron particles were accelerated by a 2MV Van de Graaff accelerator with velocities ranging between 0.8 and 40 km/s and masses between 10^{-15} to 5×10^{-10}g. Scattering of the data is visible with respect to different velocities and masses of the projectiles hitting a tungsten target. Velocities assumed values of 4, 5.1 and 7.2 km/s from the top picture to bottom one. Using the least mean square method to fit the data the mass exponent α assumed values between 1 and 0.85 for electrons and 1 and 0.9 for ions. In the same experiment the specific yield Q/m was computed as a function of the velocity of the projectile v. A strong velocity dependence with the charge yield was found and it can be seen in 2.8. where on the y axes the ratio N(I)/N(P) represents the number of ionized atom divided by the number of the atoms of the incident particle. The unitary mass m was 10^{-12}g and the coefficients were $k_+ = 0.49 \pm 0.07$, $k_- = 0.54 \pm 0.03$, $\alpha_+ = 0.9 \pm 0.15$, $\alpha_- = 0.9 \pm 0.15$, $\beta_+ = 2.7 \pm 0.4$, $\beta_- = 2.8 \pm 0.3$. The charge yield was found to be dependent on the impact angles between the normal to the target surface and the velocity of the impinging particle. The velocities investigated varied from 4 to 6 km/s using different targets. The top of figure 2.9 shows the electron charge generated by a Mo target hit by a Fe dust particle with mass $m = 6.2 * 10^{-12}$ and velocity $v = 5.1$km/s as a function of the angle of incidence Θ as shown in the top right corner. The last two plot show the total electron and ion charge released by two W target hit by Fe particles with mas $m = (13.6 \pm 1.1)10^{-12}$g and velocity $v = 5.25 \pm 0.2$ as a function of the incidence

14

angle Θ. The left bottom part of the picture shows the case of high polished W target while the right bottom one shows a $14\mu m$ thick W layer sputtered onto an Al backing
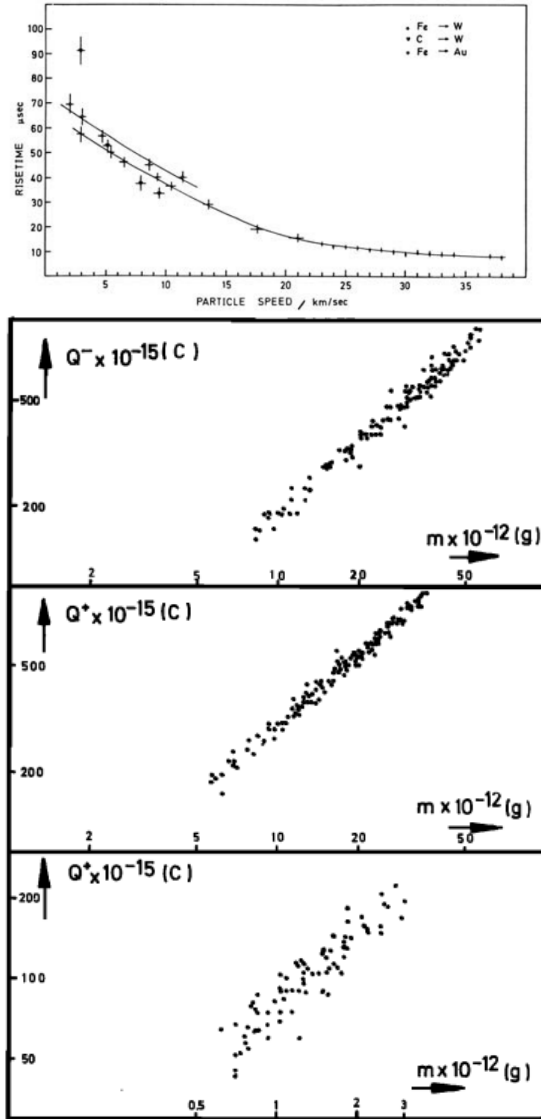
Figure 2.7: HEOS sensor rise time as function of impact velocity and the scattering of the ion charge generated by Fe particles hitting a W target.

. It is evident from data that there is a peak of emission when the incident angle is $45°$. The analysis of the incidence angle was conducted at fixed impact speed and mass of the dust particle. The ratio $Q(\Theta)/Q(0°)$, where $Q(0°)$ indicates the charge generated with an incident angle equal to $0°$, is a function $f(\Theta)$ that is the same for the mass and the velocity variation. Observing abscissa of the three plot in Figure 2.9 it is clear that the materials of the dust particle and the target play a fundamental role in the production of charge after the impact. This result was to be expected as in equation 2.1 the ratio of the densities between the target and the dust particle determines the variation of energy ΔE_H. Equation 2.11 has been accepted and used by the scientific community as a valid empiric law that well predicts the charge yield produced after a dust impact. The mass exponent α is largely assumed to be one while the material constant K and the velocity exponent β assume different value in the literature. More experiments throughout the years have tried to reproduce dust impacts that happen in space with electrostatic accelerators and, recently, A. Colette [9] compared new experimental data obtained with materials often used in space missions with some of the most reknown dust impact results published in the past. The data were collected using the electrostatic accelerator at the University of Colorado Boulder. In the first raw of the table are listed all the materials that were used as a target and the last five materials are listed to represent the STEREO spacecraft. All the experiment were conducted using iron particle as dust impacting the target with the indicated speed. The first raw of the table is the most cited formula to compute the impact.

It is evident how the charge produced using the McBride and McDonnell,[6], equation differs up to a factor of 20 for speed of 10 km/s and and up to a factor of 5 at 50 km/s. The mass exponent is equal to 1 for all materials but the velocity exponent has a minimum of 3.5 and a maximum of 5.6. Space interest materials were analyzed also by Grün and Grün at all in 1989 and 2007, [5] and [8], such as aluminum and white PCB-Z paint present on Giotto Spacecraft and BeCu present on STEREO's antennas. The table shows that except for gold all the materials that have space interest do not vary their charge yield when hit with a velocity of 10 km/s while there is a factor that ranges between 2 and 5 at 50 km/s. The material were tested at different incidence angles and the results are visible
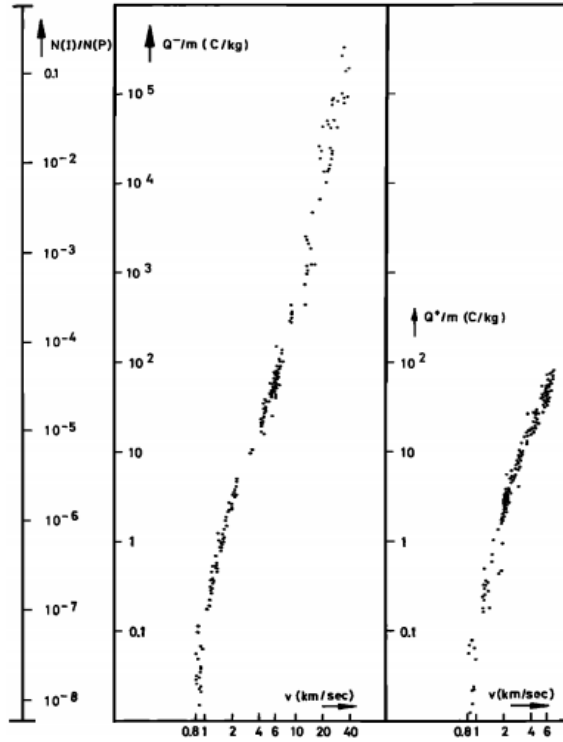
Figure 2.8: Total electron and ions charge Q normalized to the impacting mass m of Fe particles. The coefficient γ is the equal to the number of ions per number of incident atoms and it is called ionization activity coefficient.
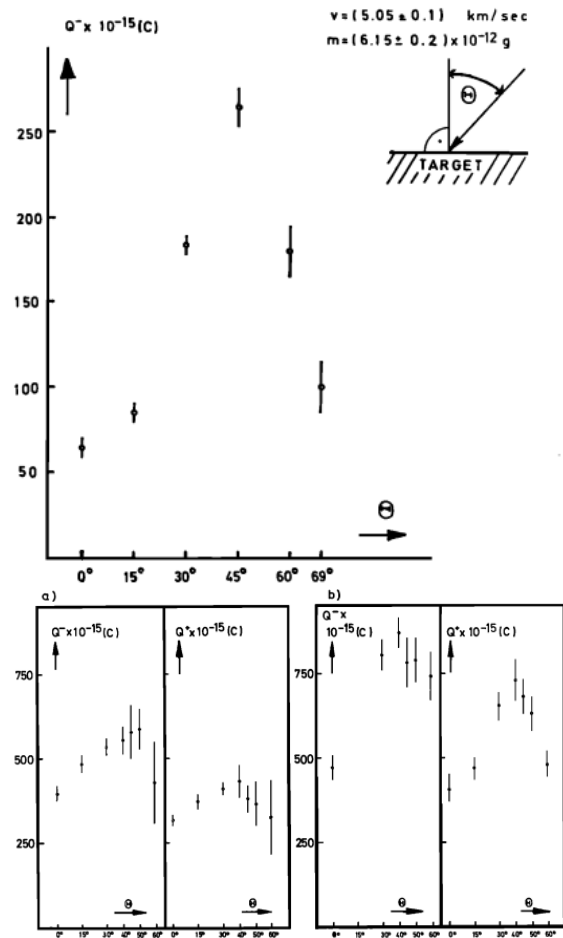
Figure 2.9: Top figure is the total electron charge Q^- released form a Mo target by Fe dust particles with a mass m = $(6.2\pm0.2)10^{-12}$g and velocity v=(5.1 ± 0.1)km/s as a function of the angle of incidence θ. Bottom pictures represent the total electron and ion charge released from two W targets by Fe dust particles with as function of the angle of incidence θ.

16
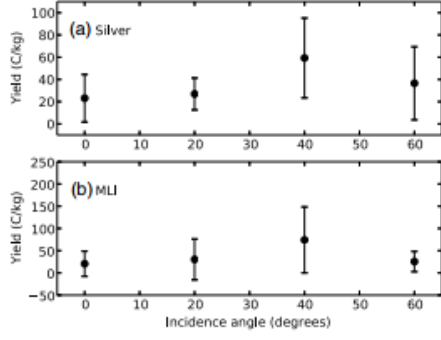
Figure 2.10: Charge yield as function of the impacting angle and target materials for Fe hitting particles with 7.5 km/s velocity.
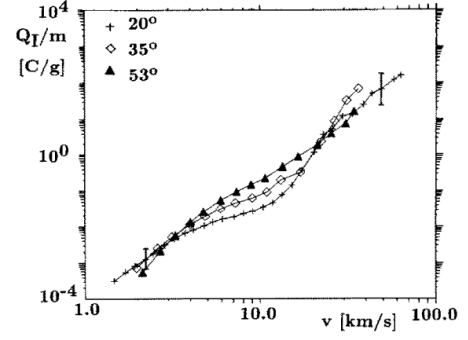
Figure 2.11: Charge yield as function of the impacting angle and velocity for Fe particles hitting a W target.

in picture were the black dot represent the average charge yield value while the bars are the standard deviation. The study was performed with 45 measurements per angle and it confirms what is represented in figure 2.9 with a peak of emission near 45° for an impact speed of 7.5 km/s. The same charge impact angle study was conducted by J. R. Göller and E. Grün [4] while calibrating the Galileo dust detector at the Max-Plank Institute. Figure 2.11 shows the charge generated by iron particle hitting a gold target at different angles. The experiment was conducted at different speeds and it is clear how the highest angle is generating the highest amount. This behaviour is the same found by Collette at all, [9], but for velocities higher than 20 km/s and lower than 5 km/s. In fact when the impact angles are out of the fore mentioned middle speed range the charge generated after the impact are equal within the uncertainty.

Target Material	Scaling Relation	Range km/s	10km/s	50km/s	Reference
Al	$7.0x10^{-1}m^{1.02}v^{3.48}$	2-40	1,060	287,000	McBride and McDonnell[1999]
W	$5.1x10^{-1}mv^{3.5}$	2-40	1,610	451,000	Dietzel at all [1973]
Al	$1.4x10^{-3}mv^{4.8}$	8-46	88	200000	Grün [1984]
Au	$6.3x10^{-4}mv^{5.6}$	9-51	2,508	20,600,000	Grün [1984]
PCB-Z Paint	$4.7x10^{-3}mv^{4.1}$	3-36	59	43,400	Grün [1984]
Antenna (Ag/BeCu)	$5.0x10^{-2}mv^{3.9}$	3-40	397	211,000	Grün at all [2007]
Kapton (Al coated)	$1.0x10^{-2}mv^{4.6}$	3-40	398	654,000	Grün at all [2007]
Polyimide	$1.2x10^{-1}mv^{3.3}$	3-45	239	48,500	Grün at all [2007]
Ag	$8.9x10^{-3}mv^{3.9}$	2-40	71	37,600	Collette at all [2014]
BeCu	$1.2x10^{-2}mv^{3.8}$	2-30	76	34,300	Collette at all [2014]
Kapton (Ge coated)	$2.5x10^{-3}mv^{4.5}$	2-40	79	110,300	Collette at all [2014]
MLI	$1.7x10^{-3}mv^{4.7}$	2-40	85	164,200	Collette at all [2014]

Table 2.1: The list of the charge impact and the data fitting constants found in the literature for material of space interest.

2.2.1 Effective temperatures

The effective temperatures of the plasma cloud generated after the dust impact is an important element that determines how many electrons or ions escape or gets captured if the target is biased with voltage. This study is important because it reproduces the floating potential of a spacecraft while in space, chapter 2. In the most recent years there have been more than one attempts that tried to measure the effective temperatures of ions and electrons but the results present uncertainties because of the complex nature of the matter. Collette at all,[10], gave a first attempt to measure effective temperatures while trying to reproduce signals captured by the STEREO spacecraft antennas after
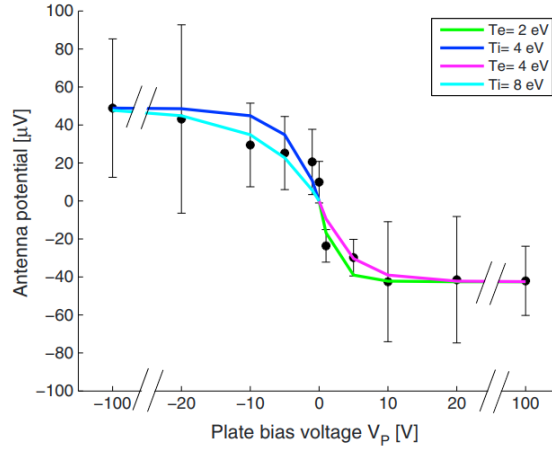
Figure 2.12: Effective temperatures of ions and electrons in eV obtained fitting the data of the measured antenna voltage.

dust impacts at LASP. Even though the primary goal of the research was to reproduce STEREO antennas signals the effective temperatures of ions and electrons were estimated assuming that the particles in the plasma, after the impact, were all leaving the target and that both species had an energetic Maxwell Boltzmann distribution. If the previous assumptions are taken into account than the antenna floating potential can be computed as a function of the bias potential applied to the target with the following formula

$$V = V_{max/min}^{\pm}(e^{\frac{\pm qV_p}{T_{i/e}}} - 1) \qquad (2.12)$$

The exponential function is the representation of the potential component of the distribution and the dimensionless exponent is composed by the elementary charge q the potential of the target V_p and the temperatures of ions and electrons respectively $T_{i/e}$ expressed in electron volts.The potential of the antenna V is readily know by measurement and the values of $T_{i/e}$ can be estimated with the fitting of the data. Figure 2.12 is the plot of the results where the black dots are the averages of the antenna potentials as function of the target potentials. The lines represent the standard deviation from the each average. The materials of the antenna is aluminum coated with graphite to make sure that the potential is as uniform as possible over the whole surface. The target was tungsten and the dust particle Iron with a velocity range between 8 and 10 km/s. The plot shows that the assumption expressed by 2.11 is confirmed in this case. In fact as the potential of the plate reaches high values the antennas measures asymptotically the same value. This means that depending on the bias voltage of the plate all the ions or electrons generated after the impact are collected by the plate. The temperatures assume values of $4eV < T_i < 8eV$ and $2eV < T_e < 4eV$. A more direct attempt to measure effective temperatures was done by Collette at all,[13], considering higher impact velocities. The results were confirming that at 4 km/s, temperatures of ions and electrons are consistent with 5eV. Data collected at 20 km/s increased impacting speed, figure 2.13, allowed The fitting of the data using a non linear least fit square with T_s and the potential of V_p of the target as fitting parameters. Differently from the previous case the charge per unit mass collected by the plate is plotted. The best fit curve shows that the temperature of the ions $T_i = 23$ eV, which is a higher value compared to lower impact velocities, and the electrons temperature $T_e = 0.6$ eV. Furthermore it is visible an asymmetry in the plot between higher negative and positive potentials that was not present at lower speeds. Kočiščák at all,[19] investigated the effect of chemical composition of the dust on the effective temperatures
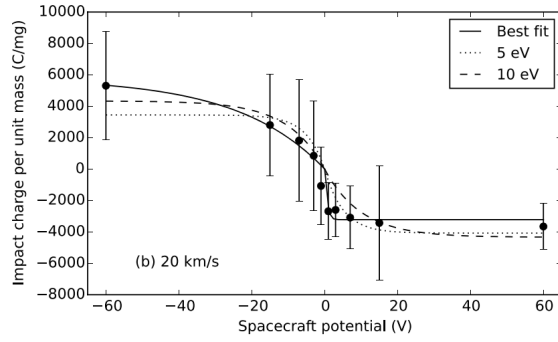
Figure 2.13: Effective temperatures of ions and electrons obtained fitting the data of Q/m collected by the target. Fe particles hit a W target at 20 km/s.
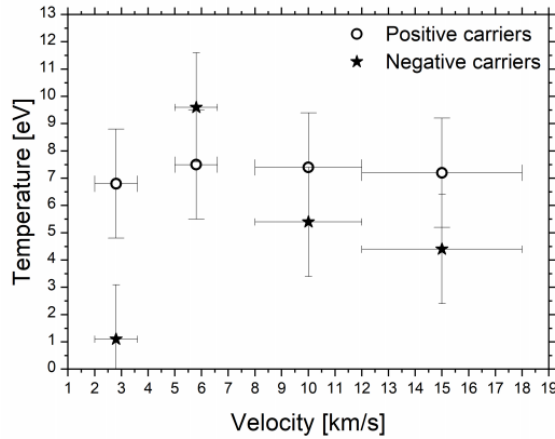
Figure 2.14: The different chemical composition of the polypyrrole dust particles hitting the W target changes the temperatures of ions and electrons particles in the impact plasma.

of ions and electrons. The incident dust grain was made of ground-up olivine, common to rock forming minerals present also in meteorites. To allow the particle acceleration a thin (<10nm) layer of conductive polypyrrole was applied on each olivine dust. The target was tungsten. At each impact the ratio between the charge collected by the W target and the mass of the dust was measured as a function of a bias potential applied to a grid facing the target. Figure 2.14 is showing the measured effective temperatures as function of impact velocities. Differently from the iron projectile case, the temperature of the ions does not depend on impact velocity and it is approximately equal to 7 eV. The presence of the thin polypyrrole layer makes the molecular composition of impact plasma more complex. Ion-molecular reaction inside the plasma may lead to the deceleration of the ions. The temperatures of the electrons is drastically different and shows a peak near 6 km/s. At lower and higher speeds the temperature is within the range of 5 eV. At the moment there is no physical explanation for the electron peak.

2.3   Conical expansion

The explanation of the conical ion expansion in this section is based on the previous work done by Tarantino et all[17] and Fletcher at [11]. To investigate the effect of hypervelocity dust impact on a spacecraft material like plate Tarantino et all performed an experimental campaign at the Max Plank Institute For Nuclear Physics. The aim of the experiment was to confront numerical simulations of the events, following Fletcher at all work, with the experimental results. The model of the plasma expansion used by Tarantino at all comprehend a multi species plasma coming out of the target after the impact. The expan-

sion phase can be divided in three stages. The first stage is a non ideal collisional plasma stage and the description is out of the scope of this work. The second and third stage are the inteparticle interacting plasma and the single particle motion stage. During the second stage plasma is dense enough to allow inteparticle interaction that can influence the entire plasma motion. In the final stage particles are independent from each other and their motion is influenced mostly by the external electric fields. The most general force acting on each particle in the plasma plasma cloud can be expressed as follows

$$\vec{F} = q(\vec{E} + \vec{v} \times \vec{B}) + m\vec{g} + m\vec{v}\nu \tag{2.13}$$

The gravity component can be neglected with respect to the Lorentz force because it is several order of magnitude smaller. The third term is the collisional term of the exchanged momentum between particles and in the last two phases considered by this model there are no collisions, hence the term can be neglected. The magnetic field present during the experiment was the Earth magnetic field and it caused the Larmor radius to be several order of magnitude grater than the dimensions of the chamber, therefore the magnetic component of the Lorentz force could be neglected like the gravitational and collisional forces. The electric field can be at this point divided into two components

$$\vec{F} = q(\vec{E}_{int} + \vec{E}_{ext}) \tag{2.14}$$

where the $\vec{E}_{int}$ is the electric field interacting between particles internal to the plasma cloud and $\vec{E}_{ext}$ is the external electric field caused by the biased target. Once the interacting force between all the different particles is known the motion a single particle can be computed numerically considering that

$$\vec{a}_i = \vec{F}_i(\vec{x}_i)/m_j \tag{2.15}$$

where i and j refer to the different species present in the plasma cloud. Before having a brief description of the integration method some assumptions must be made. The last two phases of plasma expansion behave like a gas in thermal equilibrium and the velocities inside such gas have a probability distribution. The Maxwell Boltzmann distribution was used to represent the velocity distribution along x y and z.

$$
\begin{aligned}
f_{v_{x_j}} &= \sqrt{\frac{m_j}{2\pi K_B T_j}} \exp\left\{ \frac{-m_j v_{x_j}^2}{2\pi K_B T_j} \right\} \\
f_{v_{y_j}} &= \sqrt{\frac{m_j}{2\pi K_B T_j}} \exp\left\{ \frac{-m_j (v_{y_j} - v_{by})^2}{2\pi K_B T_j} \right\} \\
f_{v_{z_j}} &= \sqrt{\frac{m_j}{2\pi K_B T_j}} \exp\left\{ \frac{-m_j (v_{z_j} - v_{bz})^2}{2\pi K_B T_j} \right\}
\end{aligned}
\tag{2.16}
$$

where K_B is the Boltzmann constant and T_j is the thermal temperature of the species after the impact. It is worth noticing how the z and y component have bulk velocities expressing the motion of the plasma.

2.3.1 Internal forces

Calculating the internal forces of a system of N particles is computationally heavy as it is of the order of $O(N^2)$ at each computational step. To reduce the computational cost to $O(N \log N^2)$ the Burnes and Hut method was implemented. As particles are loaded into the simulation at each step, the domain is divided into eight equal octants until one particle remains in each domain or a subdivision limit is reached. All the particle present in each domain are reduced to one with size and charge equivalent to those present within the cluster.

(a)

× Hydrogen
× Carbon
· Oxygen
● Sodium
● Iron
● Tungsten
● Representative

(b)
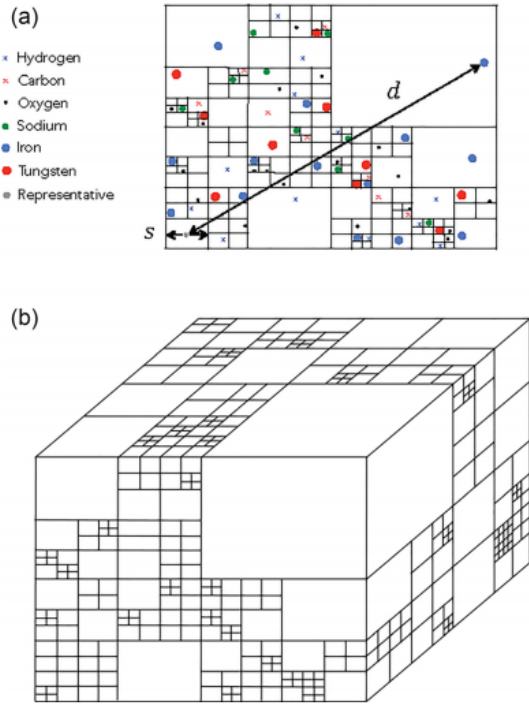
Figure 2.15: representation of the subdivision of the domain with the Burnes and Hut method.

The equivalent charge is located at the center of the cluster. This creates a treelike structure of nodes that are all connected inside the domain. At each step the octants subdivision changes as new particles enter into the simulation. In the situation just described the force of the particles inside a cluster is nearly equivalent to the force exerted by the equivalent charge located at its center. The effectiveness of this approximation is called force resolution parameter and depends on the ratio between the dimension of the subdomain s and the distance d between the particle at the center of the cluster and the particle of interest, Figure 2.15. To compute the electrostatic force between two particles the Lennard Jones formula is used

$$F = \frac{q^2 r}{4\pi\epsilon_0 \left(r^2 + \left(\frac{e_1+e_2}{2}\right)^2\right)^{\frac{3}{2}}} \quad (2.17)$$

where q is the charge of the two particles, r is the distance that separates the two charges and e_1 and e_2 are the effective sizes of the particles. The solution converges for the effective sizes approaching zero and the increasing of their distance r. Using The Lennard Jones potential allows to describe better the quantum interaction between particles and ,as it can be seen in figure 2.16, it impedes the potential to assume infinite values when the distance between two particles approaches zero. This avoids nonphysically large forces between particles during simulations. As the domain can be divided in smaller domains which dimension can span over small orders of magnitudes, μm, to large ones, cm, the length scale is divided by the Debye length and the time scale by the inverse of the plasma frequency in order to avoid rounding-off errors. The electrical permittivity and the electron charge to mass ration were set to 1. All the values computed during the simulation scaled accordingly.
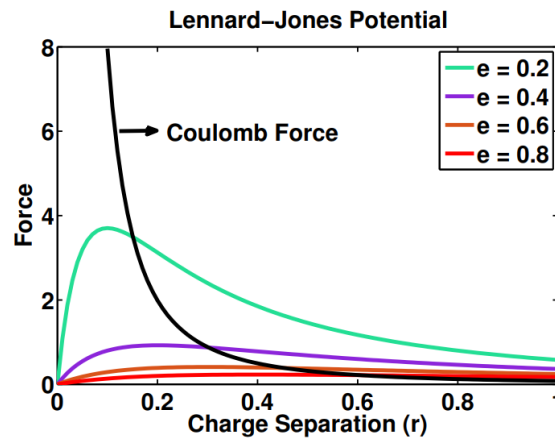
Figure 2.16: Lennard - Jomes potential plot showing the different behaviour of the force between two particles with respect to the Coulomb force.

21

2.3.2 External forces

The external force acting on the particle due to the biased target were calculated creating a CAD model of the experimental set-up inside an electrostatic solver. The values of the electric field at each point in space were imported into the plasma expansion model directly after a logarithmic grid scaling.

2.3.3 Sensor model

In order to the simulation to be complete the sensors used for the experiment had to be modeled and introduced into the simulation. The CAD model of the detector was needed to predict the current captured at each time step. The experimental set up used a series of Faraday Plate Arrays that operated as Faraday cups. The FPA has a metallic disk that collects plasma and the current generated by the hit is recorded by a fast oscilloscope with a maximum sampling rate of 2.5 gigasamples per second. The current recorded by the FPAs was simulated as follows

$$I_i = \frac{S\eta q}{\Delta t_i} \tag{2.18}$$

where q is the ion charge and η the number of particles that hit the sensor at each time step Δt. The real charge that a sensor collects at each time step was computed using the following empirical formula

$$S = \frac{Q}{qN_p} = \frac{0.1 m_{proj} \left(\frac{m_{proj}}{10^{-11}}\right)^{0.02} \left(\frac{v_{proj}}{5}\right)^{3.48}}{qN_p} \tag{2.19}$$

where v_{proj} and m_{proj} are the mass and velocity of the projectile respectively and N_p is the number of particles. In order to convert ampere to voltage the transimpedance amplifier transfer function was computed as

$$H(s) = \frac{(4 \times 10^{20})s}{(s + 16.8 \times 10^6)(s + 1.78 \times 10^6)(s + 50)} \frac{V}{A} \tag{2.20}$$

2.3.4 Results
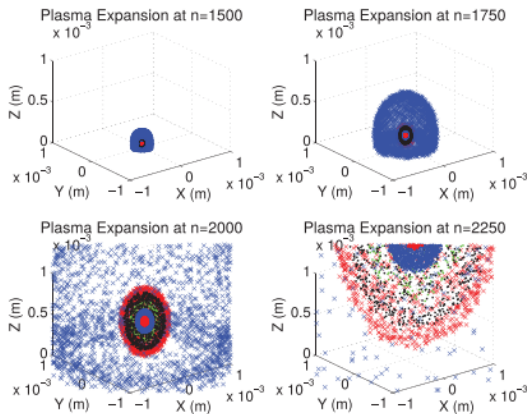
Figure 2.17: Positions of the ions at each step of the simulation show a conical shape expansion. The lighter ions occupy the largest angle and the heaviest the smaller.

The results of the numerical simulation can be observed in figure 2.17. Being the plasma composed by multiple species after the impact, the plot shows the spacial expansion of each species at different time steps. hydrogen, carbon, oxygen, sodium, iron, and tungsten are represented by the blue x's, red x's, black dots, green dots, blue dots, and red dots, respectively. It is possible to notice that Hydrogen is the less massive element of the group and is the first one to leave the impact location. The most massive element is tungsten and it leaves the target as last. The pattern of the expansion is a concentric conic shape and the lighter spices expands with the larger angle.

Chapter 3

Antenna dust detection

3.1 Floating potential

In situ dust observations are performed during missions with space dust analyzers, like the one in 2.6, or with Radio Plasma Wave Science instruments(RPWS). A. Zaslavsky [12] proposed a model that had good results explaining the waveforms captured by STEREO's RPWS and it considered a spacecraft as conductive object that acquires an equilibrium potential while orbiting in space. Because of the equilibrium voltage present on the spacecraft body impact charge can be collected by its surface when thermal energies are not enough to overcome the potential barrier. The equilibrium potential can be computed performing a balance of the currents that the spacecraft is subjected

$$\frac{dq}{dt} = \sum_{n=1}^{N} I \tag{3.1}$$

The right hand term of the equation depends on the environment the spacecraft is orbiting. The biggest contribution is given by the photoelectric current, I_{ph}, and the solar wind current, I_{sw}. The current due to secondary emission is, in most of the case negligible and it is going to be neglected. The model makes the assumption that the mean free path of the particles carrying the charges after the impact is small compared to the size of the satellite and the trajectories are determined by the spacecraft potential only. Under these assumptions the two currents can be computed as follows

$$I_{sw} \simeq I_{e0} \left(1 + \frac{\phi}{T_e} \right)^{\alpha}$$
$$I_{ph} \simeq I_{ph0} \left(1 + \frac{\phi}{T_{ph}} \right)^{\beta} e^{-\frac{\phi}{T_{ph}}} \tag{3.2}$$

Where I_{sw} is the current associated to plasma collected by the spacecraft and I_{ph} is the photoelectric emission that escape the object. I_{e0} is the current collected by the spacecraft if the voltage were to be zero, ϕ is the potential q/C where q is the charge present on the surface of the spacecraft and C is its capacitance, T_e is the the solar wind electron temperature in eV. I_{ph0} is the current generated by the photoelectric effect and can be computed as $I_{ph0} = J_{ph0} S_{lit}$ where the J_{ph0} is the current density generated by UV solar flux impacting the surface S_{lit}. The current density is the integral of the charge yield produced and a specific frequency over the whole spectrum and $S_{lit} < S$ where S is the entire surface of the spacecraft. The coefficients α and β consider the geometry of the charging object and compares it with the Debye length λ of the of the object's potential.

If the λ is small compared to the object the $\alpha, \beta = 0$ and the charging is a 1D charging. In the case of 2D charging one of the dimension of the object is grater than λ and in the 3D case all dimensions of the object are small compared to λ. For the last two cases $\alpha, \beta = 1/2, 1$ respectively. It is worth noticing that the equilibrium voltage is easily obtained because all the parameter needed for computation depend on the space environment. Considering that the spacecraft is composed by the main body and a cylindrical antenna it can be shown that the stationary form of equation 3.1 is

$$e^{\frac{-q\phi}{Tph}} = \frac{en_e v_e S}{J_{ph0} S_{lit}} \frac{(1 + \frac{q\phi}{T_e})^\alpha}{(1 + \frac{q\phi}{T_{ph}})^\beta} \tag{3.3}$$

equation 3.3 states that the equilibrium potential of a spacecraft depends on the electron density n_e, the thermal temperature of the electrons T_e and photons T_{ph}, the mean velocity of electrons v_e, the photoelectron density current J_{ph0} and the portion of the area of the spacecraft S_{lit} illuminated by the sun. These parameters make the potential of the spacecraft ϕ dependent on the plasma environment. The exponents α and β depend on the Debye length and how it compares with the dimension of the body that collects or emits the charge. Considering the 1D case in which the Debye length is small compared to the spacecraft body it is possible to compute the equilibrium potential of the spacecraft analytically (α , $\beta = 0$)

$$\phi_{sc} = \frac{T_{ph}}{q} \ln \frac{J_{ph0} S_{lit}}{en_e v_e S_{sc}} \tag{3.4}$$

considering the cylindrical shape of the antenna the Debye length is comparable with its diameter and α , $\beta = 1/2$. In this case the solution to equation 3.2 must be found numerically.

When a dust impact occurs the voltage of the spacecraft or the antenna slightly changes because of the impact charge and the current related to the dust impact must be added to the right hand term of equation 3.1. The perturbation are small if compared to the equilibrium potential and a Taylor expansion at the first order allows the computation of the perturbation of the equilibrium potential as function of time. Equation 3.1 lienarized reads

$$\frac{d}{dt}\delta\phi + \frac{1}{\tau}\delta\phi = \frac{I_{dust}(t)}{C} \tag{3.5}$$

where τ is the discharging time, C is the capacitance of the spacecraft or the antenna and I_{dust} is the current forcing term. The discharging time τ depends on the geometry of the object discharging. For the spacecraft and antenna τ can be computed as follows

$$\tau_{sc} = \frac{C_{sc} T_{ph}}{en_e v_e S_{sc}}$$
$$\tau_{ant} = \frac{C_{ant} T_{ph}}{en_e v_e S_{ant}} \left(1 + \frac{\phi_{eq,ant}}{T_e}\right)^{-\frac{1}{2}} \tag{3.6}$$

where C_{sc} and C_{ant} are the capacitance of the spacecraft and the antenna, S_{sc} and S_{ant} are the spacecraft and antenna surfaces and $\phi_{eq,ant}$ is the equilibrium potential of the antenna. The solution of equation 3.5 is a convolution integral of the kind

$$\delta\phi(t) = \frac{1}{C} \int_0^\infty e^{-\frac{t'}{\tau}} I_{dust}(t - t') \, dt' \tag{3.7}$$

where I_{dust} is an arbitrary function. Considering the Δt time as the time needed for collecting the charge after an impact the shape of I_{dust} is not relevant if $\Delta t \ll \tau$. This
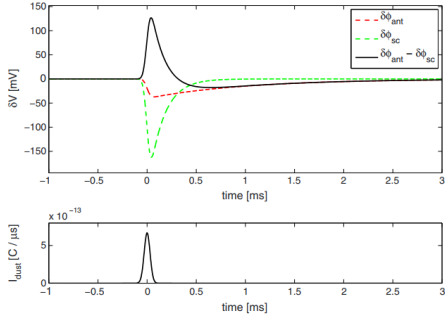
Figure 3.1: Floating potential for $\Delta t \ll \tau$
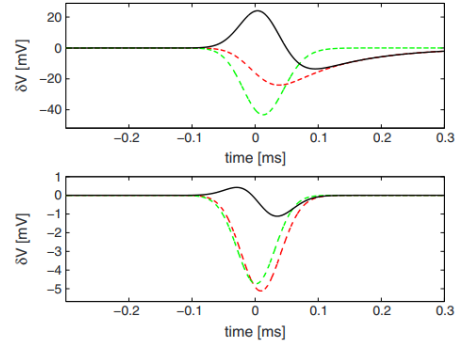
Figure 3.2: Floating potential for $\tau \ll \Delta t$

property of the convolution integral allows to arbitrarily choose I_{dust} and using a Gaussian function it would read

$$I_{dust}(t) = \pm \frac{Q}{\sqrt{2\pi}\Delta t} e^{-\frac{(t-t_0)^2}{2\Delta t^2}} \tag{3.8}$$

where the dual polarity is considering the fact that the current due to dust can be negative or positive depending the sign of the equilibrium potential. If the spacecraft is at negative equilibrium potential ions are expected to be attracted while electrons ware pushed away. Q is the charge collected and the maximum floating potential is expected to be $\delta\phi_{max} =$ Q/C and after the maximum the function relaxes depending on τ. A simple monopole antenna configuration would capture the difference in the potentials of the spacecraft and antenna

$$\delta V = \Gamma(\delta\phi_{ant}(t) - \delta\phi_{sc}(t)) \tag{3.9}$$

where δV is the voltage captured by the monople and Γ is an attenuation factor due to the electrical coupling between antenna and spacecraft. Using the relaxation times provided by equation 3.6, the same profiles for both antenna and spacecraft and solving equation 3.5 it is possible to compute δV. In some space environment it is possible that the condition $\Delta t \ll \tau$ is not satisfied and the discharging time of the conductors is faster than their capacity to collect charges. In this configuration $\tau \ll \Delta t$ and the choice of the function $I_{dust}(t)$ influences the behaviour of the voltage perturbation after the peak. The difference between the two cases can be seen in figure 3.1 and 3.2. Figure 3.1 represents the simulation of a monopole response considering Q =50 pC that is collected on a timescale of $\Delta t = 30$ μs, $C_{sc} = 200$ pF , $C_{ant} = 60$ pF, $\tau_{sc} = 150$ μs, $\tau_{ant} = 1000$ μs. The bottom plot in figure 3.1 is the Gaussian I_{dust}. Figure 3.2 top plot is the simulation where the discharging time of spacecraft and antenna are respectively $\tau_{sc} = 15$ μs and $\tau_{ant} = 100$ μs. The bottom plot considers $\tau_{sc} = 1.5$ μs and $\tau_{ant} = 10$ μs. It is evident that when $\Delta t \ll \tau_{sc,ant}$ the Gaussian shape of I_{dust} influences the rising time of the signal $\delta\phi$. The shape of the function after the peak depends on τ. Considering the case when the $\tau_{sc} \ll \Delta t \ll \tau_{ant}$, top plot figure 3.1, and $\tau_{sc} \ll \tau_{ant} \ll \Delta t$, bottom plot of figure 3.2, the shape of the voltage perturbation $\delta\phi$ is Gaussian. It is important to notice how the amplitude of the signal is drastically reduced when $\tau \ll \Delta t$. The latter case is important also when the antenna is biased with current in order to detect DC electric fields or the floating potential of a spacecraft. The current forced into the antenna is typically grater than the solar wind current. The solar wind current disappears in the balance of currents and the equilibrium voltage for the antenna reads

$$e^{-\frac{\phi_{bias}}{T_{ph}}} \simeq -\frac{I_{bias}}{J_{ph0}S_{lit}(1 + \phi_{bias}/T_{ph})^{\frac{1}{2}}} \tag{3.10}$$

25
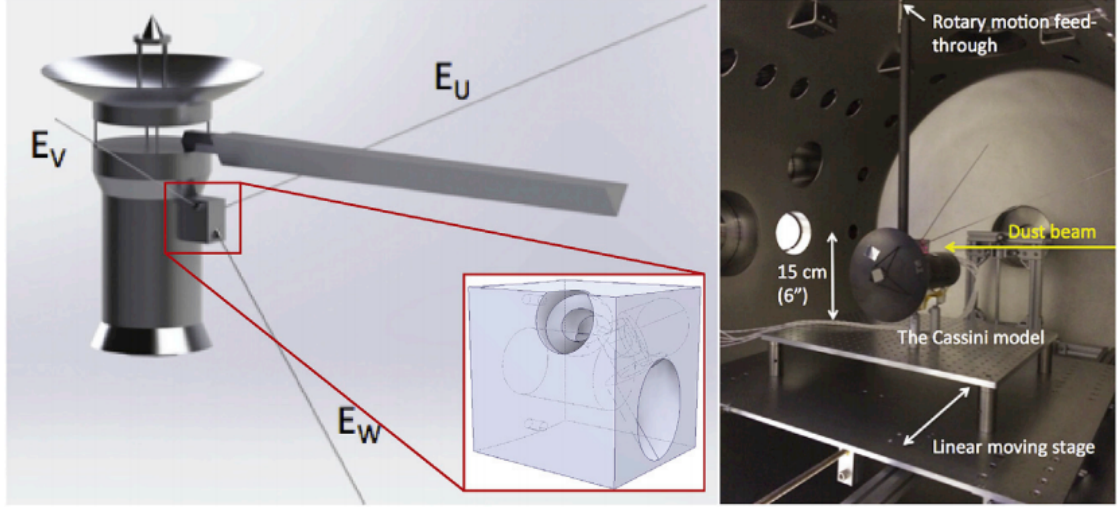
Figure 3.3: Cassini model used during the experiment inside the vacuum chamber.

It is evident how the potential of the antenna does not float with the environmental parameters and the discharging time of the antenna reads

$$\tau_{bias} \simeq -\frac{C_{ant}T_{ph}}{I_{bias}} \ll \tau_{ant} \tag{3.11}$$

The time discharge of the biased antenna is drastically reduced with respect to the unbiased case and the voltage detected by the monopole is too.

3.2 Laboratory experiments on dust impact

Zaslavsky model on floating potentials is the first model that can be adapted on different kind of environments and since the model came out there were many attempt to reproduce signals similar to those captured by Cassini and STEREO in a laboratory controlled environment. Nouzák et all [16] used a scaled down model of Cassini,1:20, to perform a shooting campaign using the electrostatic accelerator at the LASP facility. The Cassini model had three nearly orthogonal antennas like the real Cassini isolated from the spacecraft body and each other. The antennas were 50 cm long with a diameter of 1.6 mm and made out of steel. The main body was cylindrically shaped and equipped with the high gain antenna. The electronics were stored inside the main body and had a bandwidth range of 50 Hz - 400 kHz with a voltage gain of 100. Each element could be fed with bias voltage independently. The model was placed into a vacuum chamber at 10^{-6} tor and to simulate plasma present in space two resistors were placed in parallel with an equivalent resistance of 5 MΩ. The discharging constant was computed as τ=RC where C was the capacitance of each biased object. The beam entering the vacuum chamber hit a tungsten foil that could be placed in different locations. The stage the model was placed on could be moved and it was attached to a shaft that allowed rotation. The results of the experiment were useful to understand better the mechanics of the signals generated by the antennas. Some of the waveforms can be seen in figure 3.4 and all of them refers to spacecraft body hit. The tungsten foil was placed on the High gain antenna in order to prevent antenna charge recollection and the bias voltage was changed in order to observe the effect on the signals captured by the monople antenna. Observing the plots there are three different phases that characterize the antenna signal generation. The plot a shows the case in which the spacecraft body was biased with a voltage of +45V. The red rising curve is the signal

26
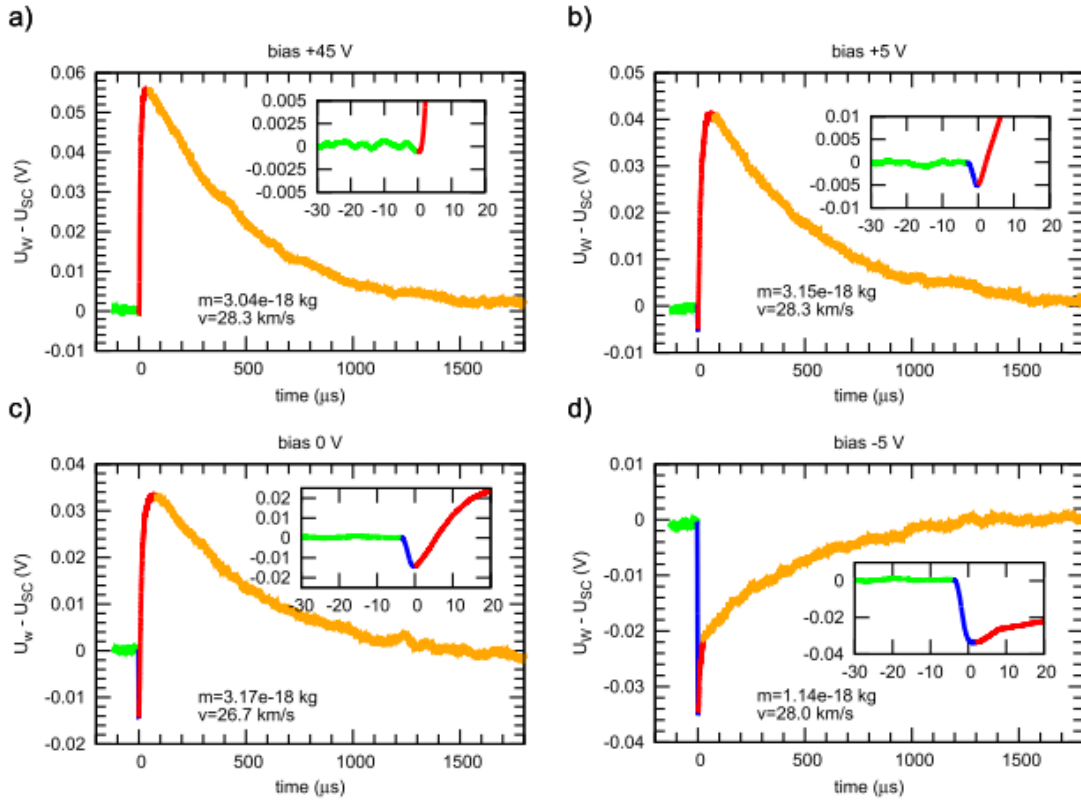
Figure 3.4: Signals captured by the monopole antenna during the experiment performed by Nouzák et all [18].

related to the escaping of ions pushed away by the positive potential applied to the space-craft. The orange curve is the negative exponential decay typical of RC circuits. The b plot represents a hit with the biased voltage reduced to +5V and a fast decreasing blue curve appears showing that some electrons have enough thermal energy to escape. The c and d plots have 0 V and -5 V potential applied to the spacecraft body. The fast decaying blue curve becomes more negative with the decreasing of the spacecraft voltage while the red rising curve becomes shorter. It is evident that at more negative potentials more electrons are pushed away from the spacecraft and more ions remain trapped. Because of the described mechanism it is evident that the polarity of signals depend on the voltage present on the conductor. If the voltage is highly positive the signal shows a positive spike. A more negative bias voltage causes a fast negative signal called pre-spike followed by a rising one. All types are followed by an exponential decay called relaxation. The raising time of the blue curve is faster than the red one because electron move faster with respect to ions.

3.3 New electrostatic model

3.3.1 Spherical model

In the previous two sections of this chapter Zaslavsky theoretical model and the latest experiment reproducing dust impact signals were explained in order to give the reader a better understanding of the phenomena. Zaslavsky's model was used to fit the waveforms of STEREO spacecraft [12] and there was a good to excellent agreement between data and fitting curves. The experiment performeb by Nouzák et all[18] was the first of his kind. Colette et all [13],[15] used a metal plate to simulate the spacecraft to obtain thermal temperatures of electrons and ions. In order to avoid geometrical uncertainties a complete model of Cassini was fabricated prior Nouzák's experiment and the results

gave a deeper understanding of the events that happen after the impact. In this section a new electrostatic model of antenna signal generation is proposed to better address the coupling capacitance between spacecraft and antennas, Γ factor in equation 3.9, and to better reconstruct the very first moments after the impact. The electrostatic model that follows is going to reproduce a signal after that a hypervelocity hit occurs on a spherically shaped spacecraft body to better compare the results to the plot obtained by Nouzák at all. Antennas signals after a dust impact can be divided in four different phases called cloud generation, electron escape, ion escape and relaxation. In the very first moments after the impact the plasma cloud is a non ideal collisional expanding plasma as the mean free path of electrons is shorter than the size of the cloud. As the expansion continues the mean free path of electrons gets higher than the plasma cloud and as last stage of the expansion the Debye length becomes larger than the size of the cloud. When the Debye length becomes larger than the plasma cloud size ions and electrons enter in a single particle motion regime and plasma divides itself into fast escaping electrons and slow escaping ions. It is possible to get a simple estimation of the dimension of the expanding sphere when electrons can be considered free from the gravitational pull of ions considering that expanding plasma is a very dense cloud of ions and electrons with temperatures of 1-5 and 5-30 eV respectively. Being in a plasma state, the overall charge of the cloud is null and the presence of the charged spacecraft does not affect the charges expanding trajectories. Considering a simple model of a spherical expansion the electrons can be considered free from ions interaction when their temperature, eV, is higher than the electrostatic potential of ions. This simple relation can be expressed with the following equation

$$\frac{T_e}{q} = \frac{Q_i}{4\pi\epsilon_0 R} \tag{3.12}$$

Where Q_i is the ion charge, T_e electron temperature expressed in electron volts, q the elementary charge and R the radius of the expanding sphere. When equation 3.12 is satisfied electrons can be considered as decoupled form the attraction of ions. Using the most conservative value for electron temperature, 1eV, and an average value for Q_i the distance R = 9 cm. Since the value of R is very small compared with the dimensions of a satellite body and antennas it is possible to think of plasma as decoupled electrons and ions that are effected electrostatically by the charged spacecraft. As plasma is the first stage of the cloud after the impact equation 1.10 holds and the number of ions is equal to the number of electrons. The conservation of charge yields

$$\begin{cases} Q_i & = Q_{i,esc} + Q_{i,coll} \\ Q_e & = Q_{e,esc} + Q_{e,coll} \end{cases} \tag{3.13}$$

Equation 3.13 states that the amount of negative and positive charge can be split into smaller portions related to the quantity of ions and electrons that are able to escape due to their thermal energy. $Q_{i,esc}$ and $Q_{e,esc}$ are the ions and electrons that have enough thermal energy after the impact to escape the electrostatic force of the spacecraft, while $Q_{i,coll}$ and $Q_{e,coll}$ are the positive and negative charge collected by the spacecraft body. Considering the energy distribution of ions and electrons a Maxwell-Boltzmann distribution it is possible to compute the amount of escaping and collected charge as follows

$$\begin{cases} Q_{e,esc} = -kQ_{imp}e^{\frac{-qV_{sc}}{T_e}} \\ Q_{e,coll} = Q_{imp} - Q_{e,esc} \\ Q_{i,esc} = Q_{imp} \\ Q_{i,coll} = Q_{imp} - Q_{i,esc} \end{cases} \tag{3.14} \qquad \begin{cases} Q_{e,esc} = -kQ_{imp} \\ Q_{e,coll} = Q_{imp} - Q_{e,esc} \\ Q_{i,esc} = Q_{imp}e^{\frac{-qV_{sc}}{T_e}} \\ Q_{i,coll} = Q_{imp} - Q_{i,esc} \end{cases} \tag{3.15}$$
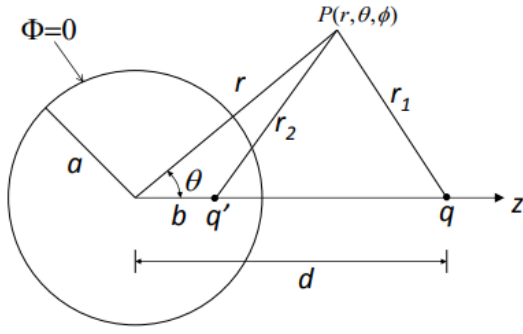
Figure 3.5: simplified example of spherical shaped spacecraft.

Equations 3.14 and 3.15 consider the cases of the spacecraft being at positive and negative potential respectively, V_{sc}. When V_{sc} is positive all ions are repelled because of the electrostatic forces and part of the electrons have enough thermal energy to escape. The coefficient k considers the geometrical configuration of the spaceraft and antennas taking into account that, in the vicinity of the spacecraft walls, ions and electrons see an infinite plane due to their infinitesimal dimension. Shen at all [20] considered, as first step of approximation, the spacecraft to be a spherical conductive shell and the antenna a passive sensor capable of detecting the perturbation of the spacecraft voltage only. Using the image method it is possible to compute the induced charge on the spacecraft caused by a test charge at a distance d from the spacecraft. Figure 3.5 sketches a point charge q at a distance d from the center of the sphere of radius a. The first step is to consider the potential of the shell of the sphere at ground, hence the boundary condition is $\Phi = 0$ for $\Phi = \Phi(r = a, \theta, \phi)$. To achieve this result an image charge q' is placed inside the sphere at a distance b from the center. As the potential in a point depends on the radial distance between the charge and the point in space it follows that

$$\Phi(r, \theta, \phi) = \frac{q}{4\pi\epsilon_0 r_1} + \frac{q'}{4\pi\epsilon_0 r_2} \tag{3.16}$$

to impose the boundary condition it is necessary to write equation 3.16 for r=a and it reads

$$\Phi(r = a, \theta, \phi) = \frac{1}{4\pi\epsilon_0} \left(\frac{q}{\sqrt{r^2 + d^2 - 2rd\cos\theta}} + \frac{q'}{\sqrt{r^2 + b^2 - 2rb\cos\theta}} \right) \tag{3.17}$$

Equation 3.17 must be equal to zero for the boundary condition to hold and rearranging the terms it possible to obtain the following condition

$$\sqrt{\frac{a^2 + b^2 - 2ab\cos\theta}{a^2 + d^2 - 2ad\cos\theta}} = -\frac{q'}{q} = C \tag{3.18}$$

condition of equation 3.18 holds if b=a^2/d and C = a/d. As b=a^2/d

$$q' = -\frac{a}{d}q \tag{3.19}$$

The image charge to make the sphere grounded is known as its distance from the center. In our case the satellite might not be at 0 potential therefore it is need to compute the solution of the induced charge for a not grounded sphere. Such solution is easily obtained imagining that there is a charge Q distributed on the surface of the spherical conductor. The grounded solution would still be valid if a second image charge, q", is placed at the center of the sphere. The sum of the image charges must be equal to Q. Hence

$$q'' = Q - q' \tag{3.20}$$

Substituting 3.19 into 3.20 the q" image charge reads

$$q'' = Q + \frac{a}{d}q \tag{3.21}$$
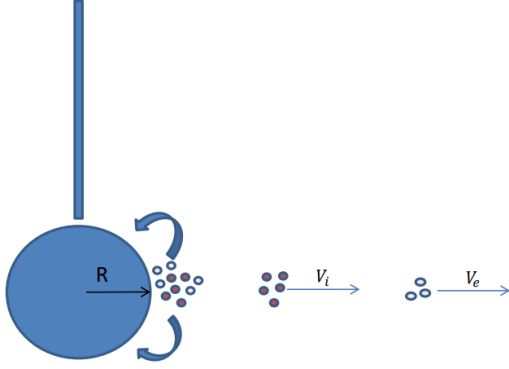
Figure 3.6: Sketch of ions and electrons expansion.

Where image charge q" is the charge induced by the charge q at a distance d from the center of the sphere. It is possible now to adapt the solution obtained with equation 3.21 to our case where the point charge is a volumetric distribution and the charges are moving and not stationary. Figure 3.6 shows a simple sketch of the case at hand. At the moment of the impact ions and electrons are equal in number, the total charge is zero, and after the expansion they behave as independent charges. The amount of escaping electrons and ions can be computed using equations 3.14,3.15 and the amount of charge induced on the sphere as they move away from the body of the spacecraft can be computed using equation 3.21. The equation that takes into account the effect of all charges acting on the spacecraft is the following

$$\delta Q(t) = Q_{e,coll} + Q_{i,coll} + Q_{e,esc}\frac{R_{SC}}{R_{SC} + v_e t} + Q_{i,esc}\frac{R_{SC}}{R_{SC} + v_i t} - \int I(t)\,dt \qquad (3.22)$$

The variation of the charge can be related to the potential perturbation through the capacitance of the sphere that is C = $4\pi\epsilon_0$R. The model considers impacts occurring on the spacecraft body only. The first two terms of equation 3.22 represent the charge Q present on the surface of the sphere because of the collected electrons and ions. The inducted charge must be proportional to the radius of the sphere and to the inverse of the distance between the escaping charges and the center of the sphere. This distance is composed by a fixed contribution R_{sc}, the radius of the sphere, and a time dependent one, $v_i t$, that represents the distance between the moving charges and the surface of the spacecraft. The induction effect goes to zero as the charges reach large distances from the center of the sphere and is equal to 1 when the charges are in the proximity of the spacecraft. The last term is the discharging term that ensures the return to equilibrium potential. Using equation 3.22 it is possible to compute the perturbation of the spacecraft potential measured by the antenna as a function of time. In fact the derivative of equation 3.22 with respect to time yields

$$\dot{\delta Q}(t) = -Q_{e,esc}\frac{R_{SC}v_e}{(R_{SC} + v_e t)^2} - Q_{i,esc}\frac{R_{SC}v_i}{(R_{SC} + v_i t)^2} - \frac{\delta Q}{\tau_{sc}} \qquad (3.23)$$

Equation 3.23 can be numerically integrated to retrieve $\delta Q(t)$.

3.3.2 System of conductors

The spherical case discussed was the starting point from where to begin to obtain a more complete model. In fact, the monople antenna configuration is composed by the spacecraft and the antenna that measures the potential difference between the two. As the antennas mounted on spacecraft are always made of conducting materials the escaping charges induction occurs on both spacecraft and antenna. Furthermore being spacecraft and antenna both conductors there is a mutual induction that is not considered by the simple spherical configuration. The antenna spacecraft model is a simplified version of a system of n conductors and the voltages on each of the conductors is linked to the charge deposited on them by the following system of linear equations

$$\begin{pmatrix} V_1 \\ V_2 \\ \vdots \\ V_n \end{pmatrix} = \begin{pmatrix} a_{1,1} & a_{1,2} & \cdots & a_{1,n} \\ a_{2,1} & a_{2,2} & \cdots & a_{2,n} \\ \vdots & \vdots & \ddots & \vdots \\ a_{m,1} & a_{m,2} & \cdots & a_{m,n} \end{pmatrix} \begin{pmatrix} Q_1 \\ Q_2 \\ \vdots \\ Q_n \end{pmatrix} \tag{3.24}$$

where the coefficients $a_{m,n}$ are called potential coefficients and the matrix contains n^2 coefficients where n is the number of equations. V_n are the potentials and Q_n are the charges deposited on each conductor. It is possible to show that the values of the coefficients $a_{m,n}$ depend on the shapes of the conductors and their relative position and that $a_{m,n} = a_{n,m}$. Being the $a_{m,n}$ matrix symmetric it is always possible to compute the inverse and the result is the matrix $b_{m,n}$. The $b_{m,n}$ terms are called coefficient of induction. The $b_{n,n}$ coefficient represents the electric quantity of the n-th conductor at unity potential when the others are kept at ground. The mixed terms $b_{m,n}$ are the coefficient of induction that describe the charge induced by the n-th conductor on the m-th when the n-th is at unitary potential and the m-th is at ground. The coefficient of induction can be expressed in terms of the real capacitance of the conductors with the following equations

$$b_{m,n} = -C_{m,n} \qquad for \quad m \neq n$$
$$b_{m,n} = \sum_{n=1}^{n} C_{m,n} \quad for \quad m = n \tag{3.25}$$

Applying equation 3.25 the system of equations 3.24 can be inverted and it reads

$$\begin{pmatrix} Q_1 \\ Q_2 \\ \vdots \\ Q_n \end{pmatrix} = \begin{pmatrix} \sum_{n=1}^{n} C_{1,n} & -C_{1,2} & \cdots & -C_{1,n} \\ -C_{2,1} & \sum_{n=1}^{n} C_{2,n} & \cdots & -C_{2,n} \\ \vdots & \vdots & \ddots & \vdots \\ -C_{m,1} & -C_{m,2} & \cdots & \sum_{n=1}^{n} C_{m,n} \end{pmatrix} \begin{pmatrix} V_1 \\ V_2 \\ \vdots \\ V_n \end{pmatrix} \tag{3.26}$$

The $b_{m,n}$ matrix in the system of equations 3.26 express a clearer physical connection between charges and voltages present on the conductors with respect to the $a_{m,n}$ matrix. The $C_{m,n}$ terms are the mutual capacitance between the conductors while $C_{n,n}$ are the self capacitance of each single conductor. Mutual capacitance depend on the geometry of the system and the shape of the conductors and can be computed with FEM simulators while self capacitance can be computed experimentally. Once the $b_{m,n}$ is available it can be inverted to find $a_{m,n}$. The equation that gives the perturbation of the potential on a single conductor can be derived by similarity from equation 3.22

$$\delta \vec{V}(t) = \underline{\underline{A}} Q_{e,coll} + \underline{\underline{A}} Q_{i,coll} + \underline{\underline{A}} \vec{g}(t) Q_{e,esc} + \underline{\underline{A}} \vec{g}(t) Q_{i,esc} - \vec{V}_{dis}(t) \tag{3.27}$$

equation 3.27 represents the most general equation for charge perturbation of a system of conductors after a dust impact occurred on the spacecraft body or the antenna. $\delta \vec{V}(t)$ contains the potentials perturbations of the n conductors where the first element is the spacecraft and the remaining n-1 elements are the antennas of the spacecraft. $\underline{\underline{A}}$ is the matrix containing the potential coefficients and it is the same for each term of the equation because nor the antennas nor the satellite change form or relative position once the final deployment in space has occurred. The quantity of the charge collected or escaping after the impact can be computed from equation 3.14 or 3.15 depending on the voltage polarity of the conductor where the hit occurs and the last term is related to the discharging current vector. $\vec{g}$ is a vector containing dimensionless elements that quantify the induced charge on each of the conductors in the system caused by the escaping electrons and ions.
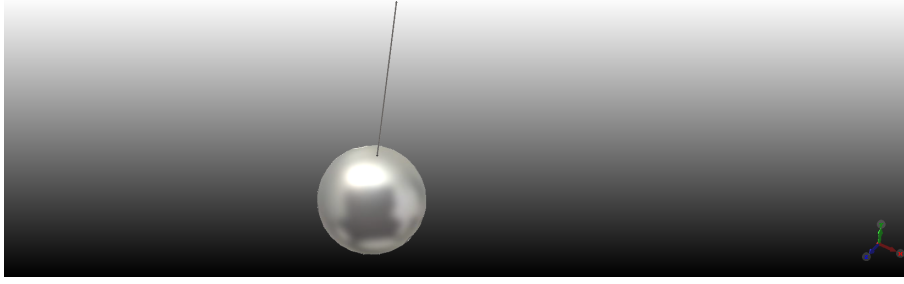
Figure 3.7: The antenna spacecraft model implemented in the FEM simulator.

It is worth noticing that the model described by equation 3.27 is an electrostatic model that allows to use the superposition effect when computing the potential. All the related effects caused by time dependent currents have been neglected.

3.3.3 One antenna spacecraft system

The simplest system to which equation 3.27 can be applied to is the antenna spacecraft system. In the spherical case the analytical solution could be found thanks to symmetry but the introduction of just one antenna isolated from the spacecraft with a cylindrical shape is making the analytical solution impossible to find. Therefore it is necessary to use a FEM simulator that is able to solve electrostatic problems. Figure 3.7 shows the implemented antenna and spacecraft model. The sphere has a radius of 76 mm and the antenna is cylindrically shaped with a length of 27 cm and radius equal to 1 mm. The materials assigned to the spacecraft and the antenna in the FEM software were perfect electric conductors and the voltage to infinite was put at ground as boundary condition. Because the conductors are two in the antenna spacecraft system the $\underline{A}$ matrix will be a square 2x2 matrix. A 0.1mm radius sphere was placed at 3 mm from the spacecraft body and it served as a 100 pC test charge distributed uniformly in the volume. A parametric sweep simulation was performed using as parameter the distance between the center of the sphere and the point charge. At each step of the simulation the voltage induced by the point charge on the sphere and the antenna was computed and the results can be seen on the top plot in figure 3.8. The x axis is measuring the distance form the point charge and the center of the sphere while the y axis the voltage. The test charge is leaving the spacecraft on a straight line at a 10° angle measured from the antenna. It can be seen that the charge is inducing more on the satellite spherical body at first because of its closer position with respect to the antenna. As the distance increases there is a crossing point where the induced voltage is the same on both conductors and it drops asymptotically to zero as the test charge goes to infinity. To quantify how much the test charge is inducing on the spacecraft and antenna equation 3.27 can be used for this particular case and the geometrical coefficients of $\vec{g}$ can be computed as follows

$$\vec{g}(d) = \frac{1}{Q_{i,esc}} \underline{\underline{A}}^{-1} \delta\vec{V} \tag{3.28}$$

The vector of the voltages contains the simulated values for the antenna and the spacecraft and $\underline{\underline{A}}^{-1} = \underline{\underline{B}}$ containing the coefficients of induction was computed by the solver during the simulations. The values of the coefficients are the following

$$\underline{\underline{B}} = \begin{pmatrix} 9.603143 & -1.431238 \\ -1.431238 & 3.269207 \end{pmatrix} pF \tag{3.29}$$
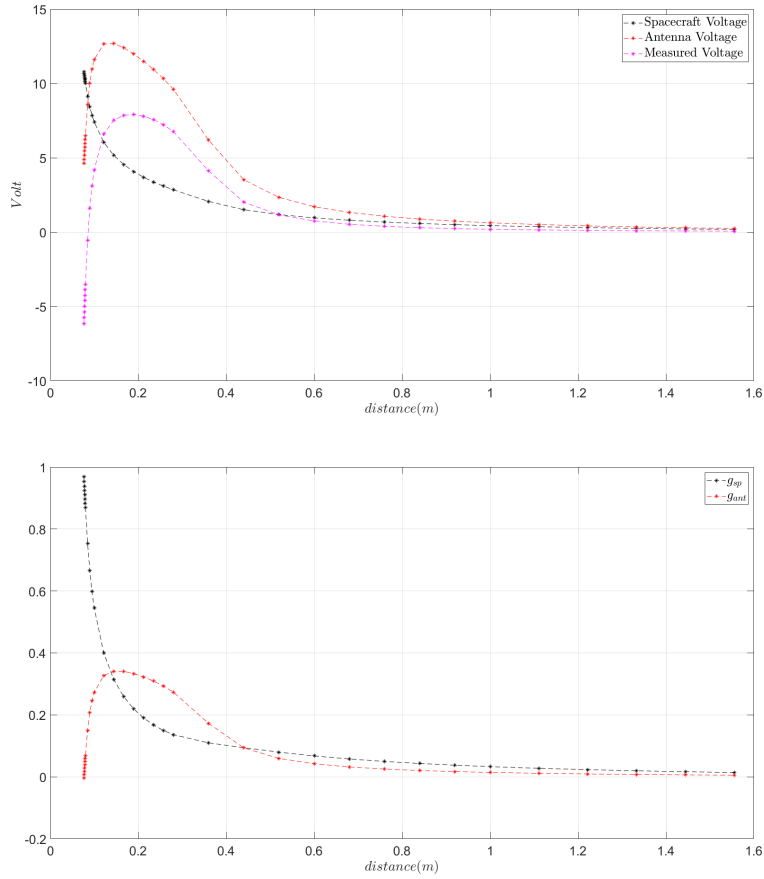
Figure 3.8: The top plot is the simulated voltage on the spacecraft and antenna induced by a 100 pC test charge. The bottom plot is the g(s) functions of spacecraft and antenna for the 10°
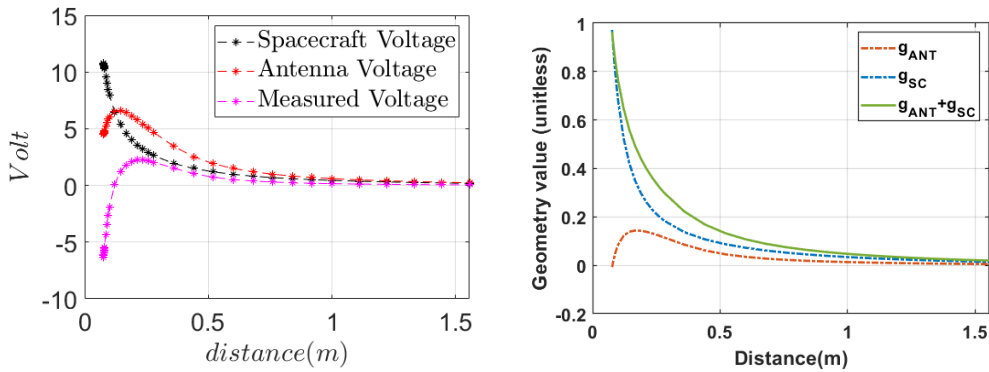
Figure 3.9: The plots are the simulated voltage on the spacecraft and antenna induced by a 100 pC test charge and the realtive g(s) functions for the 30°

The bottom plot in figure 3.8 is showing the values of the geometric coefficients for the antenna and the spacecraft as function of the distance between the test charge and the center of the spacecraft. It can be seen that $g \in [0,1]$ and $g_{sp} + g_{ant} \leq 1$. When $g_n=1$, being n the considered conductor, the test charge is inducing everything on the n-th conductor of the system and all the electric field lines leaving the charge are converging on it. When $g_n=0$ there is no induction. Figure 3.9 shows the simulated case where the 100 pC test charge is leaving the spacecraft surface at 30° from the antenna. From the two plots it can be noticed that the induction caused by the test charge does not change for the spacecraft but the value of the voltage induced on the antenna is reduces in half. This result was to be expected because the distance from the antenna was doubled. The location of the impact is of fundamental importance for the signal captured by the

antenna. The values of g_n does not remain constant like the components of the $\underline{A}^{-1}$ if the impact location changes. As last step it is possible to simulate an hypervelocity impact on the spacecraft body at $10°$ from the antenna considering all the terms of equation 3.27. Considering the $v_i = 10 \times 10^3$ m/s $v_e = 1000 \times 10^3$ m/s the velocity of ions and electrons respectively, Shen at all. [20], it is possible to switch domain from space to time. The surface of the spacecraft is in equilibrium at 0V, $Q_{imp} = 100$ pC and k = 0.5. It is possible to compute $Q_{i,esc}$ and $Q_{e,esc}$ using equation 3.14. Without loosing generality the discharging time for the spacecraft and the antenna is set to be equal $\tau = 60\mu$s.
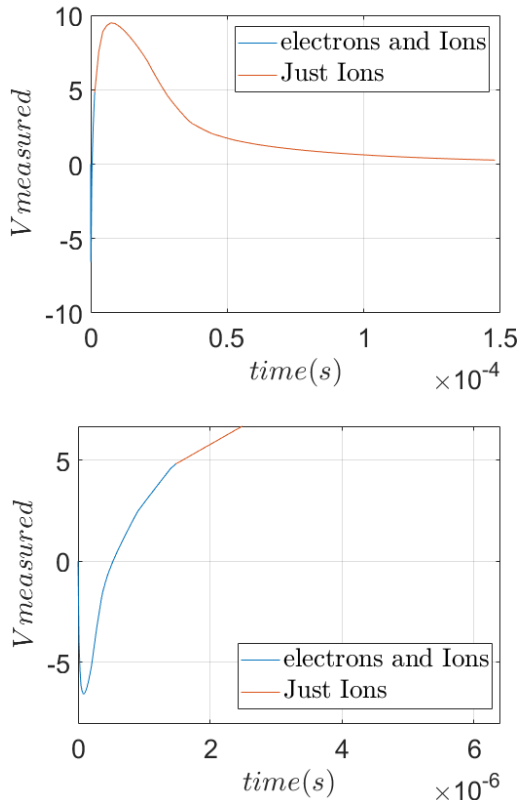
Figure 3.10: simulated monopole signal generated with the electrostatic model.

The result of the simulated impact can be seen in figure 3.10 and confronted with the 0 V case obtained by Nouzák at all [16]. experimentally. The plot shows the typical pre-spike of negative polarity followed by the positive spike. The pre-spike is associated with the second phase of the signal generation that is the expansion of the electrons. The positive peak is associated with the slow expansion of the ions. The bottom plot of figure 3.10 shows the features of the fast pre-spike. As in the 0 V case obtained experimentally the ratio between the negative and the positive spike is 0.5 which meas that the amount of electrons collected is half of Q_{imp}. After the positive peak there is the negative exponential relaxation set by the discharging time τ.The curve was plotted using two colors to identify the time when the induction effect of the fast moving electrons ends. It is possible to notice how escaping electrons and ions both induce a charge on the system for a short amount of time $\simeq 1.8$ μs. Ions keep on inducing the system for a longer time due to their lower expansion speed velocity.

3.3.4 Four antenna and spacecraft system: simulations and laboratory experiment

The signal generation model described by equation 3.27 showed capable of reproducing the shape of a signal generated after a dust impact and it was used to fit waveforms obtained during laboratory experiments. A real spherically shaped spacecraft was fabricated and equipped with four stainless steel cylindrical antennas disposed at $90°$ with respect to each other on the equatorial plane of the sphere. The size of the spacecraft body is similar to the one simulated in previous section with a diameter of 15 cm and the antennas are 27 cm long with a diameter of 1.6mm. Either the spacecraft body and the four antennas were graphite painted in order to have a constant voltage through the whole surface, Robertson et all.[7]. Two out of the four antennas operated as a monopole measuring the different potential between spacecraft and antenna while the remaining two formed a dipole antenna. The model was hanged inside a cylindrical vacuum chamber, 1.2m long with a diameter of 1.5m, evacuated to 10^{-6} Torr. The hanging mechanism inside
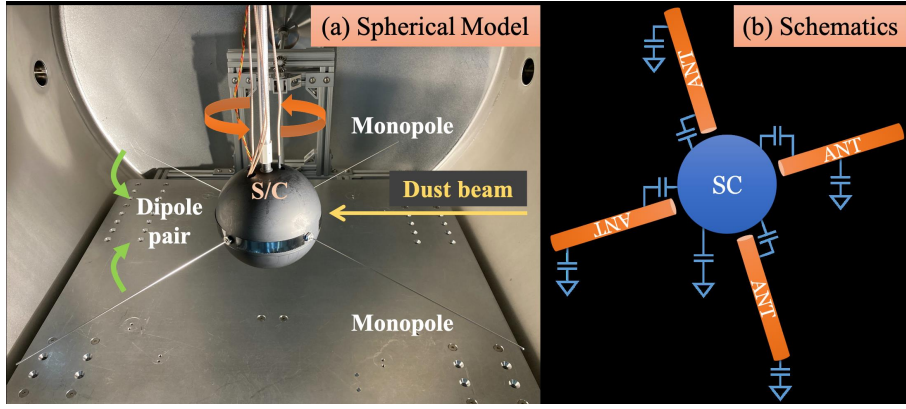
Figure 3.11: The spherical model satellite inside the vacuum chamber at LASP and the sketched capacitance circuit.

the vacuum chamber was designed in such a way that the sphere was able to rotate to change the angle of impact between the dust and the antennas while being isolated from the vacuum chamber kept at ground potential. The dust beam entering the chamber was made of iron projectiles and a tungsten foil wrapped around the sphere was the target. Differently from the simulated case the the antennas were isolated from the spacecraft through mounting brackets and electronic equipment are present to provide waveform measurements during the experiment. The electronics used for the experiment were an amplifier with a bandwidth of 270Hz-5MHz to provide a voltage gain of 50 and resistors of 5MΩ attached to the four antennas and the spacecraft to independently provide bias voltage[appendixB]. The waveforms are produced by particles with speed of 20 km/s or grater hitting the tungsten foil. In order to use the model described in the previous section the capacitance matrix $\underline{\underline{B}}$ was computed implementing the spherical model with the four rods simulating the antennas in the FEM simulator. The matrix containing the coefficients of induction reads

$$\underline{\underline{B}} = \begin{pmatrix} +11.800 & -1.2100 & -1.2100 & -1.2100 & -1.2100 \\ -1.2100 & +3.1300 & -0.0728 & -0.0267 & -0.0728 \\ -1.2100 & -0.0728 & +3.1300 & -1.2100 & -0.0267 \\ -1.2100 & -0.0267 & -0.0728 & +3.1300 & -0.0728 \\ -1.2100 & -0.0728 & -0.0267 & -0.0728 & +3.1300 \end{pmatrix} pF \qquad (3.30)$$

As expected the matrix is symmetric and it can be observed that the coupling terms of the antennas are small compared to the others. Therefore they will be neglected. The simulated $\underline{\underline{B}}$ matrix can be used to retrieve the mutual capacitance due to the geometry of the system but the self capacitance had to be measured experimentally due to the presence of many elements that were not included during the simulations such as the tungsten foil and mounting brackets. Furthermore to the geometrical mutual capacitance the electronics was creating the base capacitance that had to be taken into account.
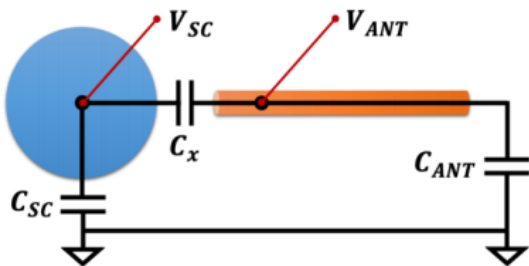
Figure 3.12: Spacecraft antenna system capacitance circuit

The one antenna spacecraft system can be used to better explain the capacitance circuit existing in the more complex model. The spacecraft has its own capacitance relative to infinite, C_{SC}, as the antenna does, C_{ANT}. Between the the spacecraft and the antenna there is a coupling capacitance, C_x, that is composed by the geometrical capacitance obtained with numerical simulations, C_G, the base capacitance, C_B, and the capacitance of the preamp, C_{WB}. It is

35

possible to compute C_x considering that C_G, C_B and C_{WB} are in parallel, hence $C_x = C_G + C_B + C_{WB}$. Hence the measured capacitance matrix is composed by the terms on the diagonal, $b_{n,n}$, representing the measured self capacitance of the spacecraft and the four antennas, the first raw and column $b_{1,n} = b_{m,1} = -(C_G + C_B + C_{WB})$ containing all measured terms of the mutual capacitance between the antennas and the spacecraft and all the other terms that are zero.See appendixA

$$\underline{\underline{B}}_m = \begin{pmatrix} +52.0 & -6.5 & -6.5 & -6.5 & -6.5 \\ -6.5 & +16.0 & 0 & 0 & 0 \\ -6.5 & 08 & +17.0 & 0 & 0 \\ -6.5 & 0 & 0 & +19.0 & 0 \\ -6.5 & 0 & 0 & 0 & +16.5 \end{pmatrix} pF \qquad (3.31)$$

as expected the coefficients are different form the simple simulated case. The term related to the spacecraft is higher and the antennas have different coefficients. A sketch of the capacitance circuit representation of the matrix $\underline{\underline{B}}_m$ is shown in figure 3.11.

The geometrical coefficients were computed as it was done for the antenna spacecraft case for three different escaping angles $10°$, $30°$ and $45°$ from antenna 1, figure 3.14. Looking at the plots of the three different cases, figure 3.13, it is evident how the escaping charges induce more on antenna 1 in the $10°$ case and the induced charge on the remaining three antennas is negligible. As the impacting angles shift towards the $45°$ case induction on antenna 1 decreases and the contribution on antenna 2 rises. The $45°$ case is the case limit where the signal captured by antenna 1 and antenna 2 is the same. The signal detected by the dipole antennas is near to zero hence the model is capable of predicting the lesser sensitivity of dipoles antenna when the impact occurs on the spacecraft body.
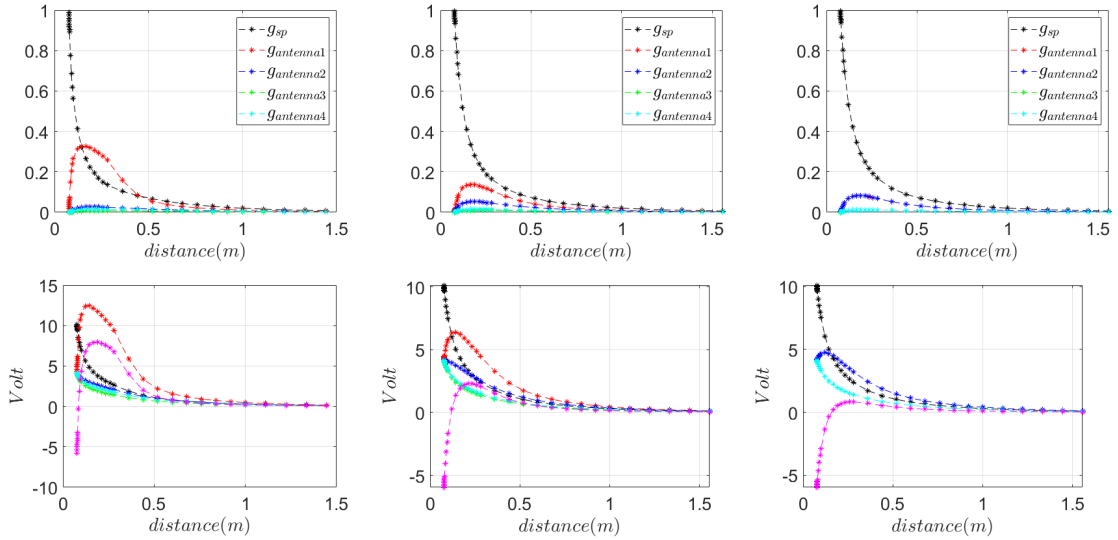
Figure 3.13: Simulated inducing function and voltages for the $10°$, $30°$ and $45°$ offset angles from antenna 1.

3.3.5 Data analysis

The experiment with the crafted spherical spacecraft was conducted to reproduce the simulation described in the previous section and to investigate the importance of the impact location in the generation of a signal after dust impact. As the spherical spacecraft was able to rotate thanks to the shaft mounted perpendicular the antennas' plane, figure 3.11, the dust beam entering the vacuum chamber could be pointed at 3 different angular distances from the monople antenna 1. The angles selected for the experiment were the
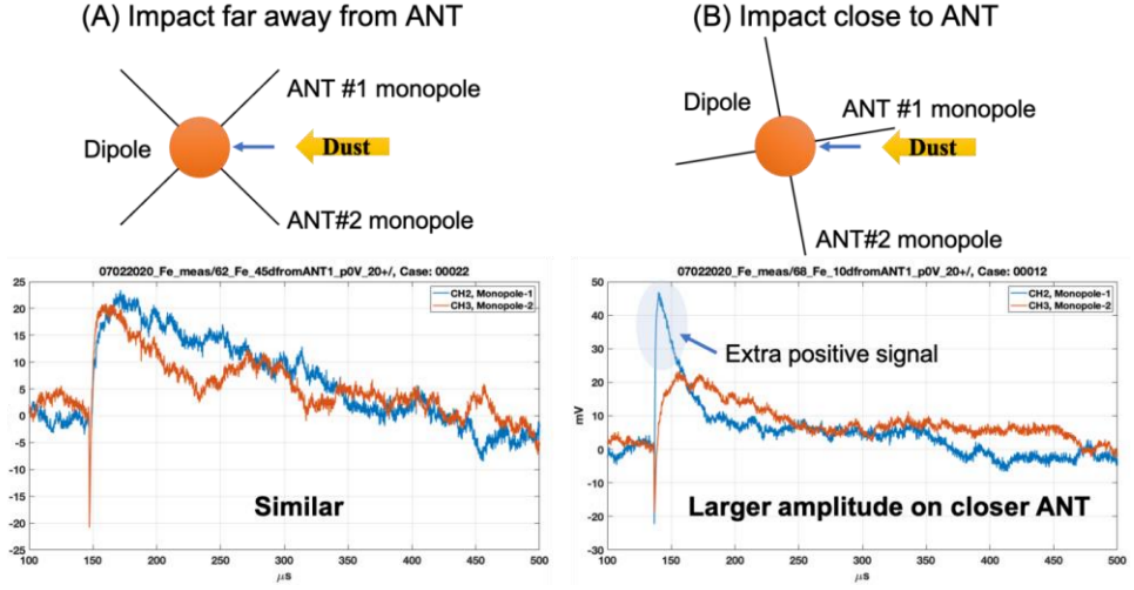
Figure 3.14: Signals generated by the spacecraft inside the vacuum chamber for the 10° and 45° case.

escaping angles of the simulated case 10°, 30° and 45°. Two of the waveforms obtained from the experiments can be seen in picture 3.14. The monopole antenna 1 measures $\delta V = \delta V_{ant1} - V_{sc}$ while the other monople measures $\delta V = \delta V_{ant2} - V_{sc}$. When the hits occurred at an angle of 45° the two signals were similar which entails that it was generated mostly due to spacecraft charging. When the impact occurred at 10°, 30° offset from antenna 1 the monople one signals had a predominant positive spike with respect to monopole 2. In this case the ions were escaping closer to the antenna and the induction effect was more efficient. The results obtained with the experiment confirmed that the electrostatic model is capable of predicting signals generated by a dust impact for different locations.

3.3.6 Fitting routine

Equation 3.27 was used to fit the waveform obtained during the experiment to validate the electrostatic model and calculate some of the parameters of the escaping plasma plume. In order to do that the capacitance matrix was used and the elastance matrix was computed as $\underline{\underline{A}}_m = \underline{\underline{B}}_m^{-1}$. The geometric functions $g(\vec{t})$ were available from simulations for all three impact locations. During the experiment antenna 2 was grounded. in this configuration equation 3.27

$$
\begin{pmatrix} \delta V_{sc}(i) \\ \delta V_1(i) \\ \delta V_3(i) \\ \delta V_4(i) \end{pmatrix} = \underline{\underline{A}}_m \begin{pmatrix} \delta Q_{sc,col} + [Q_{esc,e}g_{sc}(\vec{r}_e(i)) + Q_{esc,i}g_{sc}(\vec{r}_i(i))] - \sum_{n=0}^{i-1} \frac{\delta V_{sc}(k)}{R_{base,sc}}\Delta t \\ \delta Q_{1,col} + [\zeta_e Q_{esc,e}g_1(\vec{r}_e(i)) + \zeta_i Q_{esc,i}g_1(\vec{r}_i(i))] - \sum_{n=0}^{i-1} \frac{\delta V_1(k)}{R_{base,1}}\Delta t \\ \delta Q_{3,col} + [Q_{esc,e}g_3(\vec{r}_e(i)) + Q_{esc,i}g_3(\vec{r}_i(i))] - \sum_{n=0}^{i-1} \frac{\delta V_3(k)}{R_{base,3}}\Delta t \\ \delta Q_{4,col} + [Q_{esc,e}g_4(\vec{r}_e(i)) + Q_{esc,i}g_4(\vec{r}_i(i))] - \sum_{n=0}^{i-1} \frac{\delta V_4(k)}{R_{base,4}}\Delta t \end{pmatrix}
$$
(3.32)

The first thing to notice is that the system of equations is reduced with respect to the previous case because antenna 2 is grounded. The numerical calculations are performed with a time step Δt and the index i is used to have multiples of Δt. Hence time t = i× Δt where t = 0 is the instant of the impact. At t=0 there hasn't been any expansion yet

Figure 3.15: Simulated impulse response of the electronics used in the Spacecraft model.

and the overall charge of plasma is neutral. Hence the initial condition reads

$$
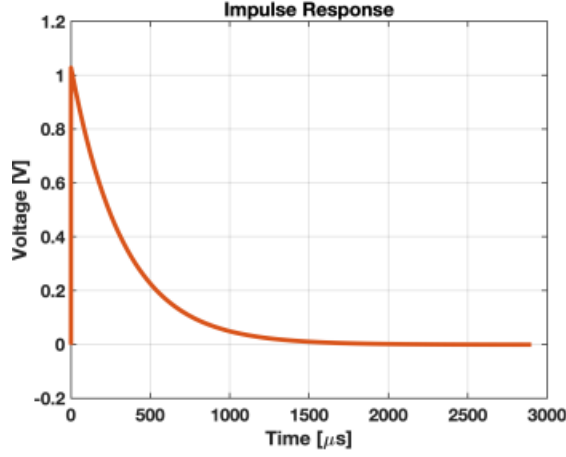\begin{pmatrix} \delta V_{sc}(i) \\ \delta V_1(i) \\ \delta V_3(i) \\ \delta V_4(i) \end{pmatrix} = \begin{pmatrix} 0 \\ 0 \\ 0 \\ 0 \end{pmatrix} V
\tag{3.33}
$$

The right hand side of equation 3.32 represents the time dependent charge on each element of the system including the collected and induced charge. The first term of each raw is the collected charge and the second term is the sum of the induced charges due to the escaping electrons and ions. As it was done in the simulations the escaping charges are multiplied by weight functions that quantify the induction on each conductor. The position vectors is $\vec{r}_e(i) = \vec{r}_{imp} + \hat{r} v_e \Delta t$ and $\vec{r}_i(i) = \vec{r}_{imp} + \hat{r} v_i \Delta t$ for electrons and ions respectively. Where $\vec{r}_{imp}$ is the position vector of the impact, $\hat{r}$ is the unitary vector of $\vec{r}_{imp}$, v_i and v_e are the escape speeds of ions and electrons respectively. The ζ_i and ζ_e are free fitting parameters for antenna 1 only as it is the closest to the impact location. These parameters allow to take into account the errors that are made because of the modeling choice to ignore the conical expansion and consider plasma as a point charge escaping radially on a straight line with constant speed. The last term of each raw is the summation of the discharging current that assumes a different form with respect to equation 3.27 because in the real case spacecraft and antennas discharge their perturbed potential through an individual resistor that is referenced to ground. As for a normal spacecraft in deep space this current will drive the potential to zero for $t \to \infty$. Solving equation 3.32 provides the time evolution of the voltages on the spacecraft and antennas. However the simulated case does not take into consideration the gain and the limited bandwidth provided by the electronics. The voltage measured by the electronics can be computed by means of a convolution integral between the physical voltages and the impulse response of the electronics. As the model is a simulated model SPICE (Simulation Program with Integrated Circuit Emphasis) software was used to simulate the impulse response of the electronics, figure 3.15.

3.3.7 Impacts at 45 deg

Figure 3.16 shows the signals for an impact location at $45°$ offset from antenna 1 where the bias potential of all the conductors but antenna 2 is zero. The two indicated signals are $\delta V_{mono,1} = \delta V_{ANT,1} - \delta V_{SC}$ and $\delta V_{mono,2} = -\delta V_{SC}$ since antenna 2 is grounded. The first thing to notice is that the two signals have significant differences since the the
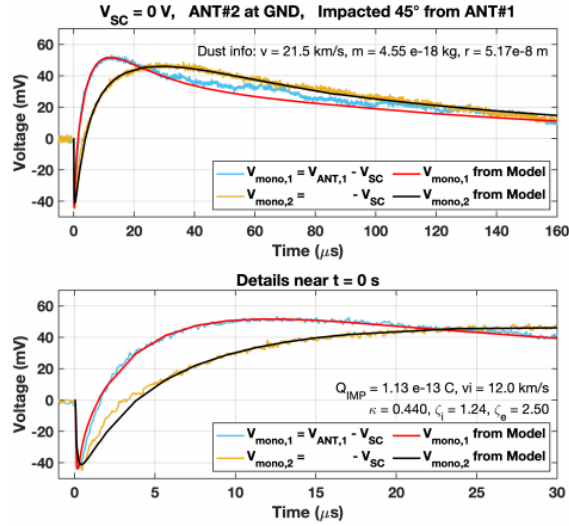
Figure 3.16: Fitting of the electrostatic model to the curve obtained during the experiment. 10° case.

maximum of $\delta V_{mono,1}$ occurs earlier in time. This means that the induced charging of the escaping electrons contributes significantly to the waveforms measured by antenna 1. Once that electrons and ions expanded beyond the length of the antenna $\delta V_{mono,1}$ captures the signal due to the charge captured by the spacecraft. Using the capacitance matrix it is possible to compute the ratio of the signal at the peak. $a_{1,1} = 2.24 \times 10^{1}0F^{-1}$, $a_{2,1} = 0.91 \times 10^{1}0F^{-1}$ and $\delta V_{mono,1}/\delta V_{mono,2} = (a_{1,1} - a_{1,1})/a_{1,1} \simeq 0.6$. The ration of the predicted value of the peaks is different from the measurement but the model is able to predict why $\delta V_{mono,1}$ drops below $\delta V_{mono,2}$ after t = 30 μs. This signal crossing has been observed for all the waveforms taken in this configuration. The start of the waveform is similar to those observed by Nouzák at all, figure 3.4. However the rate of increase of the two signals due to ion escape is different in the two signals. This is because antenna 1 senses the the induced charges of the escaping cations. This has the effect of driving $\delta V_{mono,1}$ to be more positive than $\delta V_{mono,2}$ for the duration of the cation expansion over the length of the antenna. Once the escape of electrons and ions is complete, the spacecraft is left with a negative charge. This is due to different properties of electrons and cations inside the cloud emerging from the impact plasma. While cations are expanding in the form of a plume that moves away from the impact location, electrons have an isotropic distribution. This results in half the electrons being collected by the spacecraft for the case of $V_{SC} = 0$. The spacecraft discharges thorough the bias resistor with a time constant $\tau = R_{bias}C_{eff}$. The model allows for the fitting of the waveforms to compute some of the plasma parameters such as the $Q_{imp}=1.13 \times 10^{-13}$C, k = 0.44 and $v_i = 12.0$ km/s. The latter two values are in good agreement with prior measurement, and electron expansion speed is set $v_e \simeq 10^3$ km/s, Shen at all[20]. The values of the two parameter introduced are ζ_e =2.50 abd ζ_i =1.24. The fitting of the curves would have not been possible without introducing these two parameters as the current model allows the escaping of electrons and ions at constant velocities on a straight line. The high value of ζ_e indicates that the electrons have an isotropic distribution and that a fraction of them gets closer to antenna 1 causing its charging. For the same reasoning the value of ζ_i indicates that cations move near the antenna and that they do not move on a straight line. Hence the fitting procedure shows how cations expands in from of a divergent plume rather than a narrow pencil beam. For a more detailed analysis the model is required to have a solution for the geometric function that takes into account all the locations in the vicinity of the spacecraft, and the employing of realistic models for the expansion of the electrons and ions that would also

allow calculating their charge densities as function of time and location.

3.3.8   Impacts at 10 deg

Figure 3.17 shows the set of typical waveforms for a dust impact location at $10°$ from antenna . Many features of the signal are the same of the $45°$ case The obvious difference is the much more pronounced contribution from the induced charge signal on antenna , which is the closest to the impact location. It is clear that the model does not provide as good of an agreement with the data as in the $45°$ impact location. The impact location is very near to the antenna, 1-1.5 cm, and diverging cation plume results in relatively large differences between the measurements and the simplified expansion model. As cations move in a conical expansion plume they would get closer to the antenna faster than in the case of a radial expansion moving parallel to the antenna. The result is the ambiguity determining the ion expansion speed from the fit. The best fit to the data in was done in such a way that the crossing point of the two fitting curves would coincide with the experimental data. The fitting values from the model were Q_{imp}=9.5×10^{-14}C, k = 0.43 and v_i = 10.6 km/s. Velocity and k factor are in good agreement with the $45°$ case. The ζ parameters were ζ_e =0.94 abd ζ_i =0.95 which ment that the amplitude of the waveforms were reproduced correctly by the model. Generally the model provides a good match for the entire $\delta V_{mono,2}$ and the beginning of $\delta V_{mono,1}$.
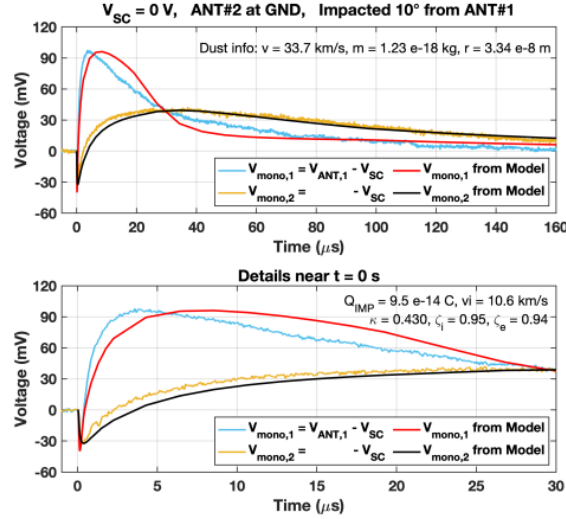

Figure 3.17: Fitting of the electrostatic model to the curve obtained during the experiment. $45°$ case.

Chapter 4

Hexanode Delay Line Detector: laboratory calibration tests

In the previous chapter the signal detected by the antennas of a spacecraft in the presence of impact plasma has been modeled as a system of conductors connected with each other by the capacitance matrix B. The model relies on electrostatic only and the induced charge of the escaping ions and electrons is treated separately considering the huge difference in velocity. The model, although produces good fitting curves as shown in figures 3.16 and 3.17, presents some problems when the dust hit the spacecraft at base of the antenna. In equation 3.27 the escaping trajectory of the positive charges is thought to be a straight line but in reality they escape in a conical shaped plume. Computing the angular distribution $\theta = \Theta(v)$ where v is the impact velocity of the dust and Θ the semi-aperture of the expanding ion plume would allow to complete the electrostatic model described in chapter 3. In order unveil the expanding trajectories of the expanding ions, three different experimental set up were proposed. The electrostatic accelerator at the Colorado University of Boulder was used in combination with a Three-Layer Delay-Line Anode detector. The aim of the following chapter is to calibrate the detector to the accelerator and propose improvement to the 3 set up described in this work.

4.1   Electrostatic accelerator

An accelerator is a machine that is capable of accelerating charged particles to very high speeds and are used to perform nuclear experiments. The Large Hadron Collider in Geneva is a circular particle accelerator that during the first collisions, in 2010, achieved energies of 3.5 teraelectronvolts (TeV) per beam. The amount of energy achieved during experiments performed with accelerators depends on the velocity of the particles inside the beam. The order of magnitude of the velocity imprinted by an accelerator on a particle varies with the kind of accelerator used for the experiment. Dust impact experiments at the LASP facility in Colorado are conducted using an electrostatic accelerator that performed its first experiment on the 14th of February 2011. The accelerator is composed by seven components, the pelletron shell,the dust source, the acceleration tube, the detectors, the deflector plates, the final detector and the target chamber. The pelletron shell can reach 3 MV potential and it works like a Van der Graaf generator. The difference between the two is that the rubber strip carrying the positive charges from the source to the shell is substituted with a chain made of metal pellets connected with insulating material. The dust to be accelerated is stored inside the dust source at high vacuum condition and it can contain any kind of conducting material or insulators coated with conducting paints. Inside the source the
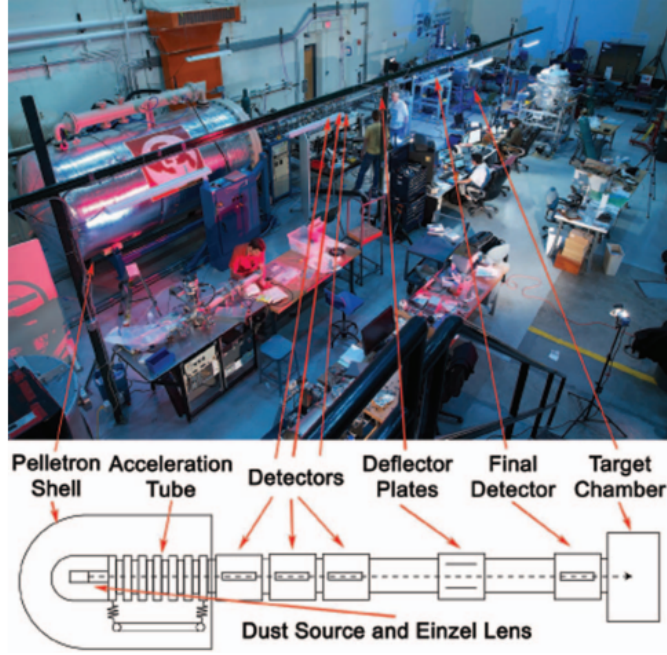
Figure 4.1: Schematic of the electrostatic accelerator at the LASP facility in Boulder.

voltage is not constant but pulsates between 0 and 20 kV relative to the extraction plate. At the very center of the source there is a needle made of conductive material that is held at constant voltage by a DC source and represents the location with the highest voltage inside the source. When the voltage between the needle and the source is low the particles are attracted by the needle that charges them as soon as they are touched. The difference in potential between the particle and the extraction plates accelerates the dust that enters into a series of concentric insulated metallic rings where the drops of the potential is linear. The metallic rings system is the acceleration tube. Dust particles encounter a series of three
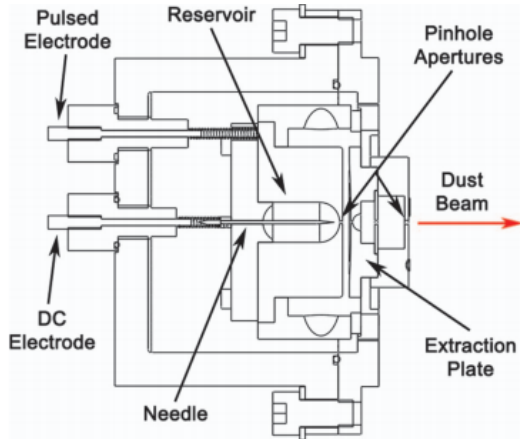
Figure 4.2: The schematic of the dust source of the electrostatic accelerator at LASP

detectors as they exit from the acceleration tube. The task of these detectors is to reveal the charge and the velocity of each particle. The charge is computed thanks to the image charge induced into the inner cylinder that is measured by a Charge Sensitive Amplifier. Velocity is deduced with the time of flight needed between the first and the last detector. Knowing the velocity and the charge it is possible to compute the mass of the particle simply with the conservation of energy. The kinetic energy of the particle is equal to the electrostatic energy acquired thanks to the pelletron shell. The detectors are used in combination with the deflector plates that impede an unwanted particle to reach the vacuum chamber. The dust in the source has a mass distribution and the conservation of energy reads

$$m = \frac{2QU_p}{v^2} \tag{4.1}$$

where Q is the charge of the particle, U_p the potential of the pelletron and v the velocity of the particle. In order to let the desired mass particle into the vacuum chamber a range of
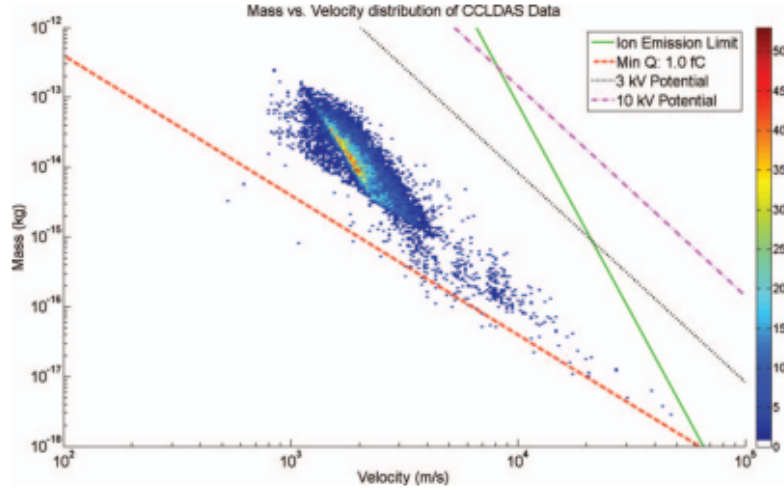
Figure 4.3: Mass to velocity distribution of the first experiment conducted by the electrostatic accelerator at LASP.

velocities and charges must be selected. All the particles with higher or lower masses with respect to the selected range are automatically discarded by the accelerator. The velocities and the charges of all the particles that passes through the plates are checked again before entering the chamber by the final detector. The charge detected is proportional to the square of the radius of the dust and the mass is proportional to the its third power. Because of equation 4.1 it follows that

$$v \propto \sqrt{\frac{q}{m}} \propto \sqrt{\frac{1}{r}} \qquad (4.2)$$

the chain of proportionality means that the fastest particles are going to be the smallest and they will have the smallest charge that is more difficult to detect. Because of this the accelerator has a lower limit which is represented by the red curve in the mass velocity plot in figure 4.3. The lower limit can be computed with the following equation

$$m = \frac{2qU_p}{v^2} \qquad (4.3)$$

where q = 1 fC which is the lowest charge detectable by an oscilloscope due to noise, U_p is the pelletron potential and v is the velocity of the particle. The green line is the ion field emission limit that represents the velocity upper limit considering a spherical shaped particle and it can be computed as follows

$$m = \frac{36\pi}{\rho^2} \left(\frac{2U_p\epsilon_0 E}{v^2} \right)^3 \qquad (4.4)$$

where ρ is the density of the dust and E is the ion field emission limit measured in volts per meter and depends on the dust material. The remaining black and purple lines are the maximum potentials that a particle can be charged inside the source by the needle and they can be computed as follows

$$m = \left(\frac{48\pi^2}{\rho^2} \right) \left(\frac{2\phi\epsilon_0 E}{v^2} \right)^{\frac{3}{2}} \qquad (4.5)$$

where ϕ is the potential of the needle. It is important to notice how the rate at which a specific particle with a specific mass enters the vacuum chamber cannot be selected by the user of the accelerator. It is possible to reconstruct a statistic of the particles that enters the vacuum chamber. In fact considering the plot in figure 4.3 it is possible to compute the mean velocity, 2.3 km/s, the maximum velocity, 52 km/s, and the standard deviation velocity, 1.4 km/s. The same information can be obtained about the mass.
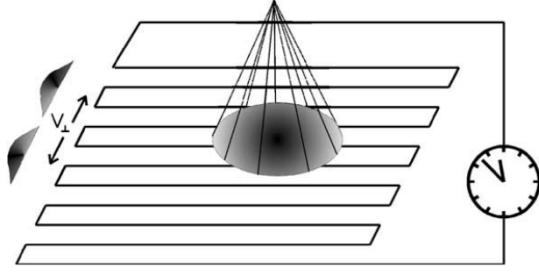
4.2 Hexanode Wire Delay Line Detector

Figure 4.4: Hexanode detector working principle.

The detection of the hit location of a photon or ion can be carried out with microchannel plate detectors with at least 2 layers of delay line anodes. The working principle of these detectors is represented in figure 4.4 and relies to the fact that when a charged particle hits a conducting wire a signal travels through the wire in both directions and $v_\perp$ is the effective velocity of the signal which is different from the velocity of the signal inside the wire. Depending on the location of where the particle hit the wire the arrival time at both ends will be different. Measuring the time of arrival of both signals one can retrieve the location of the impact. Delay line detectors need 2 lines in order to reconstruct a 2D image but the detector used for the experiment has three lines hence the name Hexanode. Each line has a twisted pair of cables that wound around isolating rods at the edge of an hexagonal base. The lines are 1 mm distant from each other and oriented with a $60°$ angle relative to each other. Each pair of a single cable has the signal and the reference wire. The reference wire is at 300 V relative the exit of the MCP while the signal cable is at a more positive voltage, usually 50 V, in order to attract more electrons. The (X,Y) coordinate of the hitting location of a charged particle with respect to the center of the detector can be computed with the following equations

$$
\begin{aligned}
u &= (x_1 - x_2)v_\perp \\
v &= (y_1 - y_2)v_\perp \\
w &= (z_1 - z_2)v_\perp + o
\end{aligned}
\tag{4.6}
$$

where x_1, x_2, y_1, y_2, z_1 and z_2 are the time of arrivals of each signal and o is an offset parameter to insure that the u, v and w are 0 at the center of the detector. u, v and w are hexagonal coordinates and it is possible to switch to a Cartesian system using the following equations

$$
\begin{aligned}
X_{uv} &= u \\
Y_{uv} &= \frac{1}{\sqrt{3}}(u - 2v) \\
X_{uw} &= u \\
Y_{uw} &= -\frac{1}{\sqrt{3}}(u + 2w) \\
X_{vw} &= (u - w) \\
Y_{vw} &= -\frac{1}{\sqrt{3}}(v + w)
\end{aligned}
\tag{4.7}
$$

It is also true that

$$
T_{sum} = x_1 + x_2 = y_1 + y_2 = z_1 + z_2 = C
\tag{4.8}
$$

In fact the time needed by a signal to get from one end to the other of a wire does not depend by the (X,Y) location and it is constant. It is possible to define a Time Of Flight (TOF) which is the time of arrival of the MCP signal t. It is possible to notice the redundancies of equations 4.6, 4.7 and 4.8. Redundancies can be used for consistency

checks and also to compute the location of a hit in case one of the signals gets lost. In case the x_1 signal is missing the X position can be computed observing that

$$u = (2y_2 - T_{sum})V_\perp \tag{4.9}$$

The same equation is valid for the other channels. In case of an outside trigger the TOF can be computed as follows

$$TOF = x_1 + x_2 - T_{sum} = y_1 + y_2 - T_{sum} \tag{4.10}$$

Hence it is possible to recover the position of the hit with just one signal registered for each layer. The detector can reveal multiple hits as well. In order to describe the multiple hit recording process a few definitions are needed. The signals captured must be converted by a Time Digital Converter (TDC) that has a dead time Δt_e. Typically it is a value around 10 ns. Δt_{pp} is the difference in time between two consecutive hits. There are three possible cases. If $\Delta t_{pp} > T_{sum}$ the position of the two hits is recorded with no additional effort. If $T_{sum} > \Delta t_{pp}$ the positions can be retrieved using equations 4.9 and 4.10 to verify which one of the signals belong to the first hit or if the signals arrive within Δt_e. The last and final case is when $\Delta t_e > \Delta t_{pp}$. The Hexanode has a region that correspond to a circle of diameter $2\Delta t_e v_\perp$ called dead region. When a multiple hits occurs inside this circle there is no possibility to reconstruct the event.
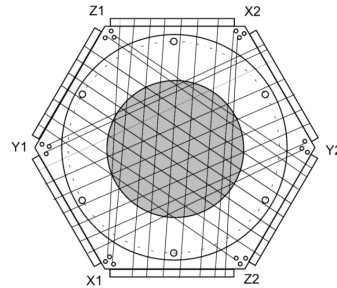

Figure 4.5: The schematic of the of a delay line anode

Position resolution depends on the resolution of the relative time resolution when information is not recovered. In case the position of the hit needs to be reconstructed the resolution drops because depends on the precision of T_{sum}. However the position resolution of this method is superior than any pixel arrangement and there is less electronics. The avalanche of electrons comes out from circular MCP stack in chevron configuration that is made of porous material with $25\mu m$ holes. For the purpose the MCP stack has a hole at its center with a diameter of 6.4mm making the active inner diameter 9 mm. The front and back plate of the stack are separated by isolating circular materials such that they can be fed with high voltages separately. The whole structure is held by an hexagon made out of aluminum called the holder. The holder is placed between the anode and the MCP stack and if it were to be put at ground potential it would effect the trajectories of the charged ions traveling inside the detector. The holder is fed with high voltage in order not to modify the flight path of ions. The tube passing through the MCP stack is made of conductive material and it must be at the same voltage of the front plate of the MCP in order to avoid fringing fields between the hole and the high voltage part of the detector. Picture 4.6 is showing the delay line anode inside the clean room while it was being readied for the experiment. The anode layers can be clearly seen under the metallic holder that is

Figure 4.6: The delay line detector inside the clean room.

45

Figure 4.7: Mounting and cabling for one corner of the detector inside the vacuum chamber.

Figure 4.8: The picture shows all the components of the experiment and the location of the feedthrough

sustaining the MCP stack. The white isolating circles are dividing the front and the back plate and the two cables are high voltage cables that feed the stack.
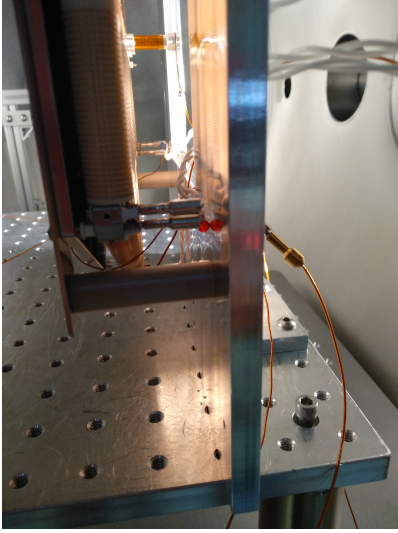
4.3 Experimental set up

The experiment was conducted in three different versions. In all three versions the MCP was mounted on an aluminum plate with a hole in the middle in order to let the cabling through. The plate was 26.67 cm tall and 20 cm large and four cylinders made out of peak divided the mounting plate from the delay line detector. The four cylindrical peaks isolated the delay line detector, where high voltages were present, from the rest of the components that were at ground potential. In figure 4.7 it can be seen the mounting design and one of the pins that captured the signals traveling through the delay lines. There were six pins, one for each corner of the detector and each one of them was connected to the feedthrough of the chamber that connected the vacuum side with the air side. Attached to the feedthrough there were in total six twisted pair of cables that carried out the necessary signals to compute the hit location of ions. The cables carrying the delay line signals were fabricated with equal length and to match the impedance between the voltage source and the MCP to avoid signal reflections. From the air side to the vacuum side of the camber there were three cables that brought high voltage to the plates of the stack and the holder. The inner hole of the detector served as pathway for the charged particles coming from the dust source to a 25×25 mm tungsten foil placed in front of the MCP stack, figure 4.8. The target foil was supported by an aluminum plate 21 cm tall and 12 cm large such that the center of the foil was at the same height of the center of the inner hole of the detector. As impacts occurred ions traveled towards the MCP that revealed the hit locations. The plate holding the tungsten foil was screwed to the base plate that allowed to modify the distance between the target and the MCP by 1 cm per hole. Attached directly to the air side of the feedthrough a signal decoupler provided the adequate connection to an amplifier with six output LEMO socket cables and at the same time it provided the necessary voltage for the reference U_{ref} and U_{sig} to the wires of the delay line through SHV inputs. The amplifier was connected directly to the decoupler and received the 6 signals from the delay lines of the detector through LEMO socket cables. It had the capability

of amplifying signals in the range between noise level and 100mV to a maximum of 2V of both polarities. The amplification was linear until 1.5 V. The rack mount case could host 8 individual bipolar amplifiers with a bandwidth of 80 MHz, the last two channels, 7 and 8, were designed specifically for the MCP signal and their bandwidth was increased to 120 MHz. The output amplified signals were sent into a constant fraction discriminator in order to reduce the jittering of an incoming signal up to a factor of 100. The input LEMO socket cables provided negative signals that did not exceed -2V and each channel of the rack could provide 3 different NIM-Out signals. The NIM signals were sent to a time to digital converter that recorded digital waveforms that were displayed on a computer using a dedicated software named COBOLT. The last connections to be described are the high voltage connections going from the air side to the vacuum chamber. The high voltage was sent to the detector by a dual high voltage supply module through SHV cables. The front panel of the power supply allowed the regulation of the voltage with two nobs and a digital reader displayed the voltage. On one of the side two switch set the polarity of each channel.
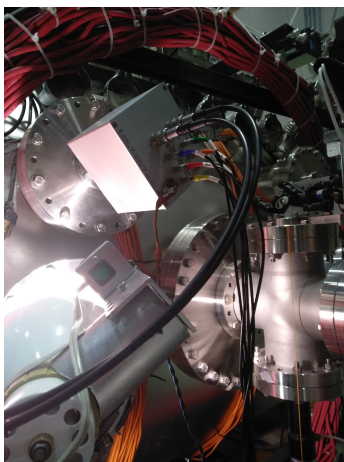

Figure 4.9: Signal decoupler attached to the vacuum chamber feedthrough.

One of the two cables of the high voltage from the power supply was connected to a passive voltage distributing unit that, through a chain of special diode, provided intermediate potentials in steps of 28V or 56V to all the components of the detector excluded the front plate. Two out of the four output SHV cables were sent to the decoupler, figure 4.9, described before to provide U_{ref} and U_{sig} to the delay lines. The remaining two SHV cables gave the appropriate potential to the holder and the back plate of the MCP. The front plate of the MCP was given high voltage directly from one of the cables of the voltage supply. The three SHV cables providing voltage to the holder, front and back plate of the detector are sent into the vacuum chamber through high frequency decouplers. The high frequency decoupler connected to the front plate of the MCP is provided with a LEMO output cable that feeds the amplifier with the MCP signal. Prior to pumping down the vacuum chamber a series of tests were performed to ensure that all the wiring connections air side and vacuum side were done correctly. The six LEMO socket cables carrying the detector signals were connected to a digital oscilloscope to make sure that noise was present and the distance peak to peak noise was less than 1 mV. If noise was too high or absent there were problems with the cabling inside the vacuum chamber. The resistance between the SHV input cables of the decoupler was checked to be grater than $10M\Omega$ to ensure isolation between the back and the front plate of the MCP. A pulse signal generator was used to send pulses inside each one of the six LEMO input channels. If the wiring inside the vacuum chamber had been done correctly the pulse going in from the x_1 channel had to come out the x_2 channel. The same thing had to happen for the other channels. If this had not been the case the layers of the delay line were not independent revealing the presence of a wrong connections. Once all the tests were performed and gave positive results the vacuum chamber was pumped down to 10^{-8} torr at a paste lesser or equal than 50 mbar/s and the detector was left for at least 24 hours in vacuum conditions before applying any high voltage. After 24 hours the high voltage was turned on and the values on each component of the detector are shown in
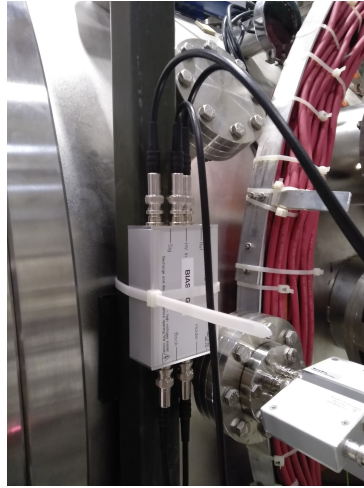
Figure 4.10: dual high voltage supply unit

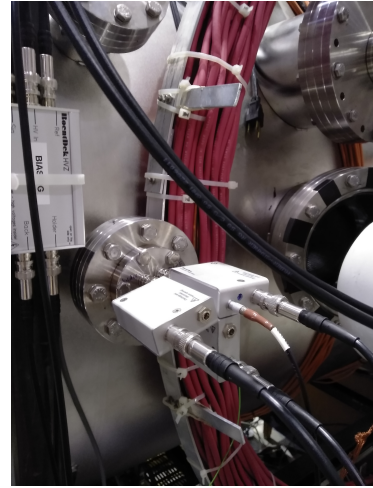Figure 4.11: Voltage distributing unit

Figure 4.12: high frequencies decouplers

the following table table. Quantities inside the table are standard values for ion detection

Component	Voltage
MCP front	-2500 V
MCP back	0 V
Delay-line anode Holder	56 V
U_{ref}	224 V
U_{sig}	274 V

Table 4.1: The table indicates the settings of the Hexagone delay line detector used for the calibration tests.

with an hexagonal MCP delay line detector and for such values the MCP stack provides a minimum voltage gain of 10^7, the detector provides $< 0.1mm$ spacial resolution, $< 0.2\mu s$ temporal resolution and a rate capability of 1 MHz. As all detectors, the MCP delay line detector device once operative showed dark counting, which are casual events determined by the temperature at which the detector is operating. Using dark counts it was possible to make the calibration of the detector to ensure it was working properly. In fact dark counts are evenly distributed on the active area of the detector if it is working properly. Figure 4.13 shows two spectrum of the same detector. The active surface of the detector was divided on the x and y axis in beams of $1.5e^{-1}$mm and the color bar on the left is showing the legend on how many causal events due to dark counts occurred in a specific x,y coordinate. The axis of the spectrum are also showing the layers from were the signals are received. The spectrum shows clearly the disk of the detector with the hole in the middle. On the left bottom of the spectrum there is the counter of the number of the total casual hit reconstructed by the first and third layer. If the top spectrum is confronted with the bottom one in figure 4.13 it is evident when the detector is not working properly. The bottom case was obtained enclosing the MCP delay line detector into an aluminum box. The purpose of the box was to stop the electric field interfering with ion trajectories. As the set up with the aluminum box was causing the detector not to function properly it was discarded. The calibration went on using the detector without the box and in figures 4.14 4.15 and 4.16 is shown the spectrum of the summation of the signals x_1, x_2, y_1, y_2, z_1 and z_2 for a beam 1e-1 ns wide. While the spectrum referring to the first and third line show a constant value in the middle beam, the spectrum relative to the second line shows unexpected pikes. The reason for this behavior was found sending
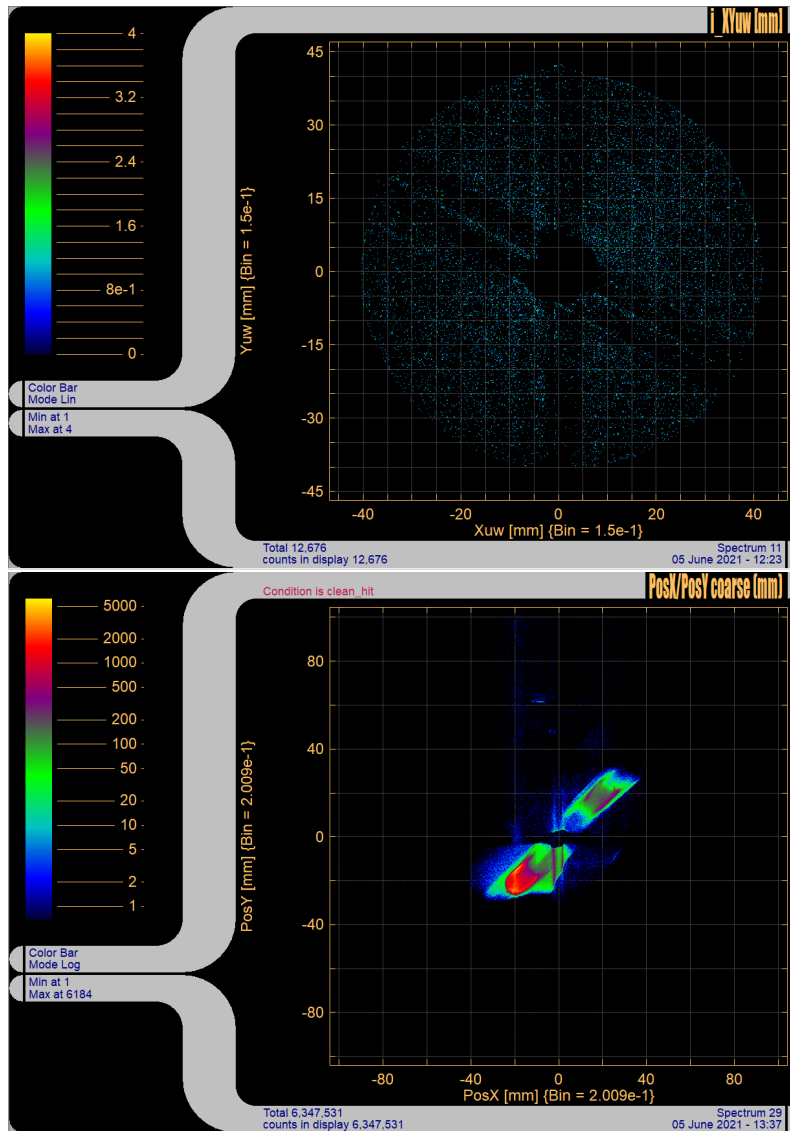
Figure 4.13: The top spectrum was taken without any metal box surrounding the detector and shows the hollowed circle of the active area of the MCP stack. The bottom picture shows the spectrum of the detector with a metal aluminium box surrounding it.

the amplified signal into an oscilloscope. As the discriminator must receive only negative signals, positive components would indicate a reflection. Figure 4.17 shows three curves. The blue one is the MCP signal coming out of the high frequency decoupler, the yellow curve is one of the signals of the first delay line of the detector, x_1, and the red curve is showing the y_1 signal. The MCP and the yellow curves show nothing out of the ordinary, while the red curve shows an abnormal negative bump 100 ns after the first one. Furthermore, there are several positive component present along the y_1 signal. The most probable cause was thought to be a wrong cable connection. Although all the test on wiring gave positive responses, all the twisted pair of cables connecting the corners of the detector to the feedthrough of the vacuum chamber were substituted but the problem was not solved. Another probable cause could have been the proximity between the aluminum mounting plate sustaining the detector and the pins collecting the signals, figure 4.7. As the remaking of the entire hardware of the internal chamber would have cost days of work and the spectrum could be retrieved using 5 channels out of 6 it was decided to carry on with the experiment using the available working channels. The calibration proceeded trying to produce ions impact on the MCP without turning on the accelerator to verify if
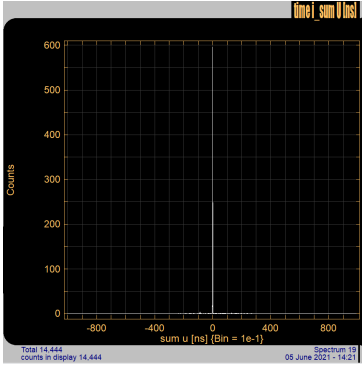
Figure 4.14: Spectrum of the summation of the signals x_1 and x_2 of the first delay line
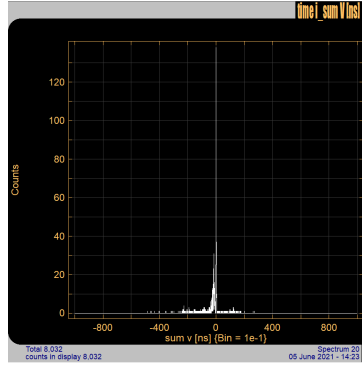

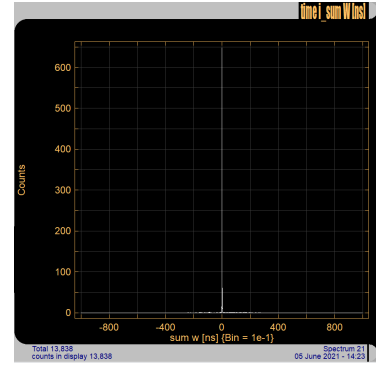Figure 4.15: Spectrum of the summation of the signals y_1 and y_2 of the second delay line

Figure 4.16: Spectrum of the summation of the signals z_1 and z_2 of the third delay line

the detector was able to catch actual impacts despite the y_1 channel missing. In order to obtain ions hits with the accelerator shut down the ion gauge inside the vacuum chamber was turned on. The presence of ions inside the chamber was certain and the setting of the experiment were left unchanged. The result of this last calibration test is visible in picture 4.18. The experiment was conducted for the same amount of time and the detector shows an increase of total hits registered. The spectrum is uniform and it does not indicate any region of the active area that was hit at a bigger rate with respect to another. This kind of result was expected as the ion gauge lets ions run free inside the vacuum chamber and the causal events do not concentrate on a specific section of the active area of the detector but they are evenly spread out. These calibration were carried out for another set up that saw a metal shield in front of the detector with a 50 % open area filter. This set up of the
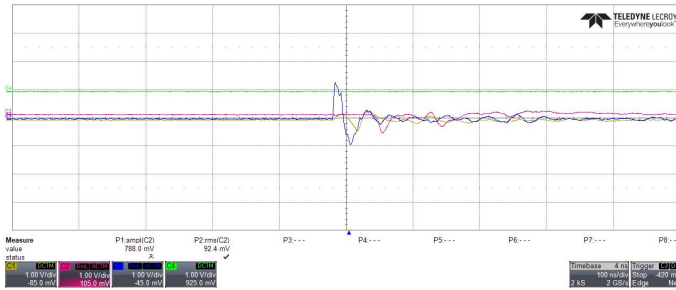

Figure 4.17: The MCP, x_1 and y_1 signals were sent into a digital oscilloscope that revealed a probable reflection on the y_2 channel, red curve.

experiment was brought up as the version with the aluminum box did not meet the necessary requirements during calibrations. On the other end, all the calibrations with the metal screen in front of the detector did not show any abnormality.

4.4   Results

In order to accelerate the dust in the source, the accelerator voltage was gradually increased until it reached the value of to 2.2 MV.The point of the needle was at 20 kv above the pelletron to create the difference in potential necessary to accelerate the dust. During the campaign 20000 micron-sized particles reached the dust chamber and hit the tungsten foil. The top of picture 4.20 shows the plot of the mass, expressed in kg, of each particle and the relative velocity in km/s. The red line was computed using equation 4.4 considering $\rho = 7.860$ kg/m^3, the density of iron, E $= 10^{10}$ V/m, $U_p = 2.2$ MV. The yellow line is the detection limit that depends on the sensitivity of the oscilloscope and was computed using 4.3 with q = 10 fC. The second plot is the kernel probability distribution of the entire campaign. The mean velocity and mass values were $v_m = 6.7378e+03$ km/s and $m_m =$
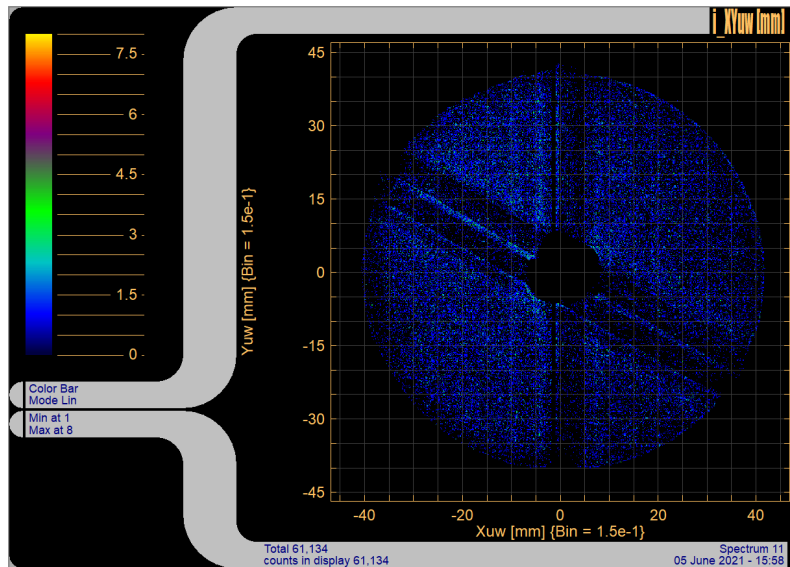
Figure 4.18: This spectrum was taken without any metal box surrounding the detector with ion gauge turned inside the vacuum chamber. The increase of the number of the hits shows that the detector is capturing real hits and not just casual events
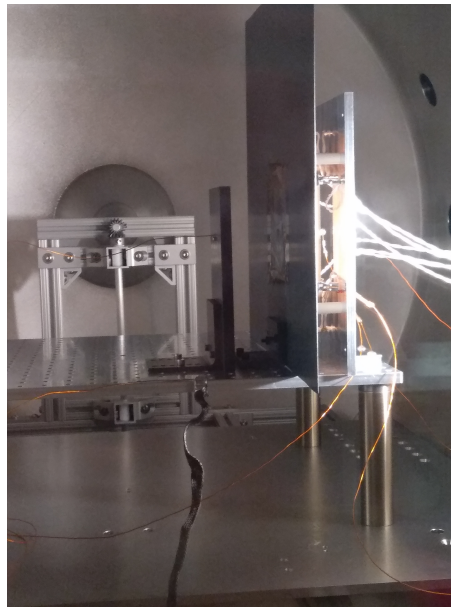

Figure 4.19: An aluminum shield is placed between the detector and the tungsten target. The distance between the MCP stack and the shield is 3 mm while the distance between the stack and the tungsten foil is 30 mm

2.2145e-15 kg with standard deviation of $\sigma_v = 5.3200e+03$ km/s and $\sigma_m = 1.9765e-14$ kg respectively. The plots in figure 4.20 confirm that the shooting frequency diminishes as the velocity increases and the mass diminishes as stated in equation 4.2. The only limitation given to the detectors was 1 km/s as bottom velocity. The top spectrum in picture 4.21 was obtained with the tungsten target at a distance of 35 mm from the the MCP stack. The image does show an increased hit rate near the cylindrical tube at the center of the disk suggesting that the the distance between the tungsten foil and the detector was too small. The duration of this part of the experiment was 1 hour and the casual events were 80/s, hence 288000 hits were due to noise. The total hit count was more than 4e+6 events, 331,332 of which captured by the spectrum reconstructed by the first and third line. The bottom spectrum of figure 4.21 shows the spectrum obtained moving the tungsten foil at 17 cm from the MCP stack.The red spot indicates that there was an increase of hits in
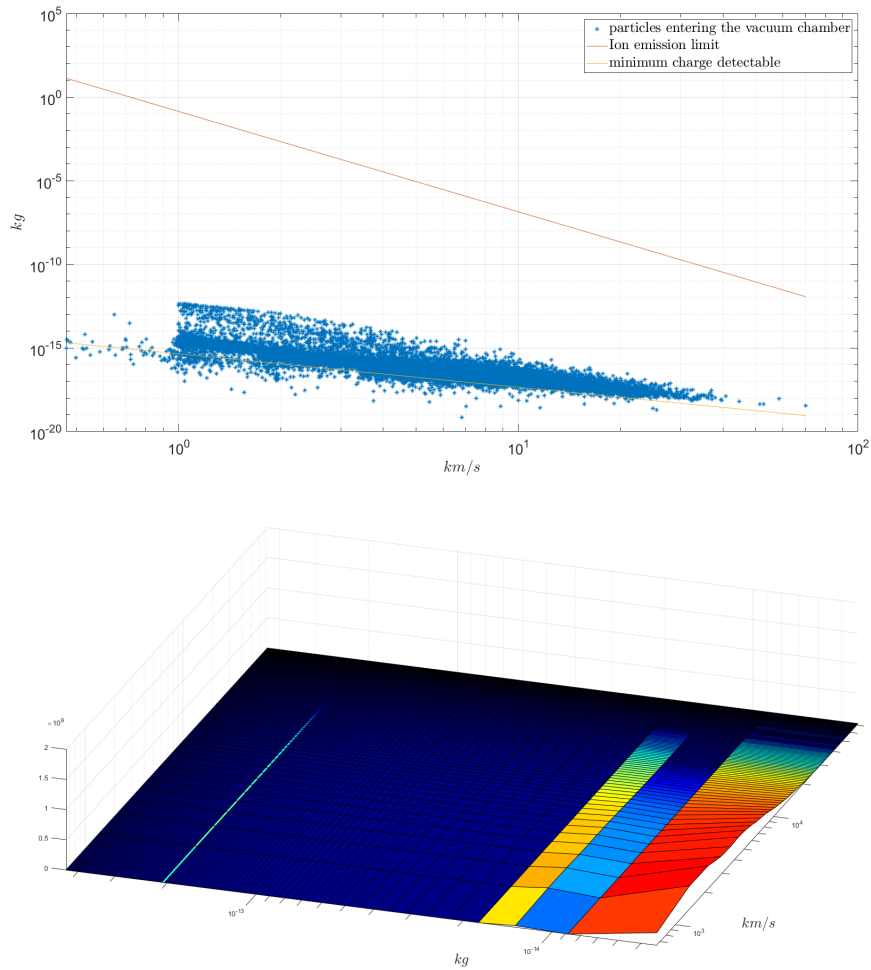
Figure 4.20: The top picture is the plot of the 20000 particles that hit the tungsten foil. The bottom picture is the kernel distribution function of the campaign.

the region near the tube. Picture 4.22 is showing the side view of the same spectrum. The spike on the left of the center hole of the detector shows where ions hit with a higher frequency. The region appear to be of conical shape with a base diameter of 10 mm. The spike on the right side of the detector might indicate the presence of ions in the region of the central area but due to the presence of the tube further investigations are needed. The last configuration of the experiment was conducted with an aluminum shield at a distance of 3 mm from the plate of the stack. Such distance was chosen in order not to have electrical discharges. The aluminum shield had a circular hole that covered the whole active area of the detector. The filter was made of stainless steel with an open area of 50% and was taped on the aluminum shield. The tape was graphite painted in order to avoid charging due to ions hit, figure 4.19. The results can be seen on the spectrum in figure 4.23 and id does not show any significant result. The same configuration was used biasing the tungsten foil with a 5V in order to push ions towards the MCP and attract electrons on the target. No significant results were noticed. Events events per second were slightly above noise it is most probable that the filter reduced the amount of ions hitting the front plate.

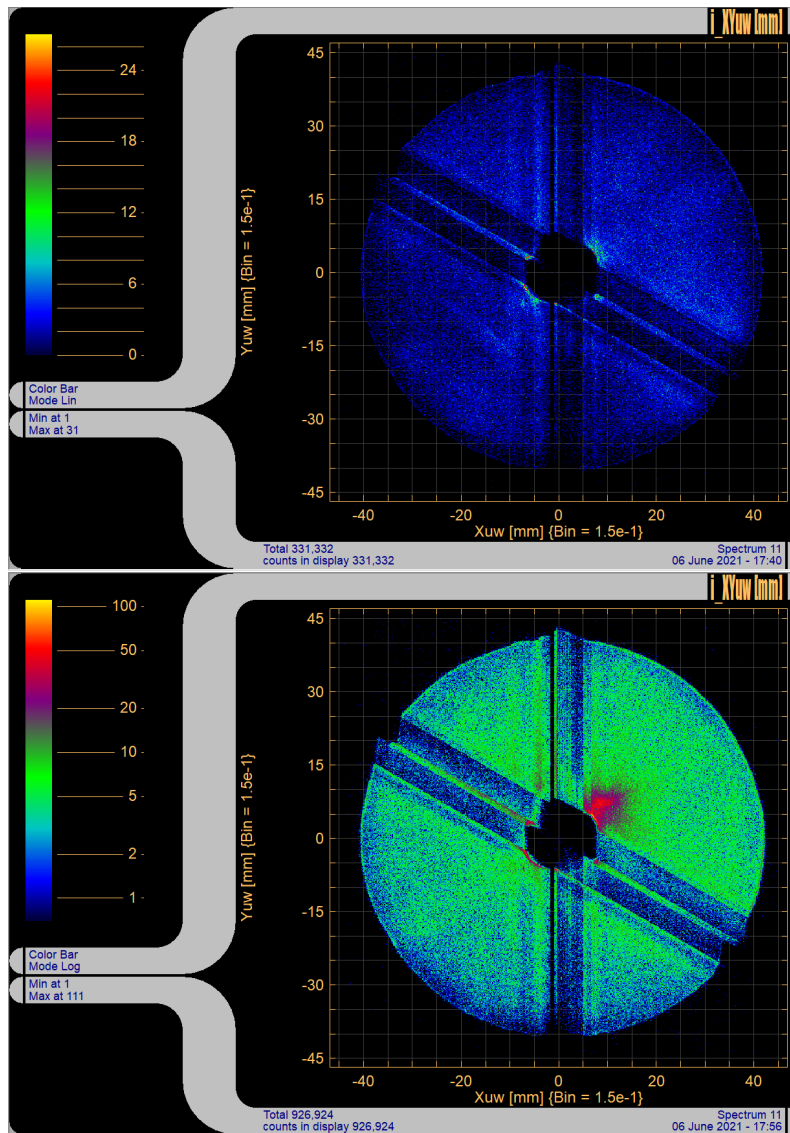Figure 4.21: The top picture is spectrum of produced by the detector with the tungsten target at 35 mm. The bottom spectrum was acquired with the tungsten foil at 17 cm from the tungsten foil.
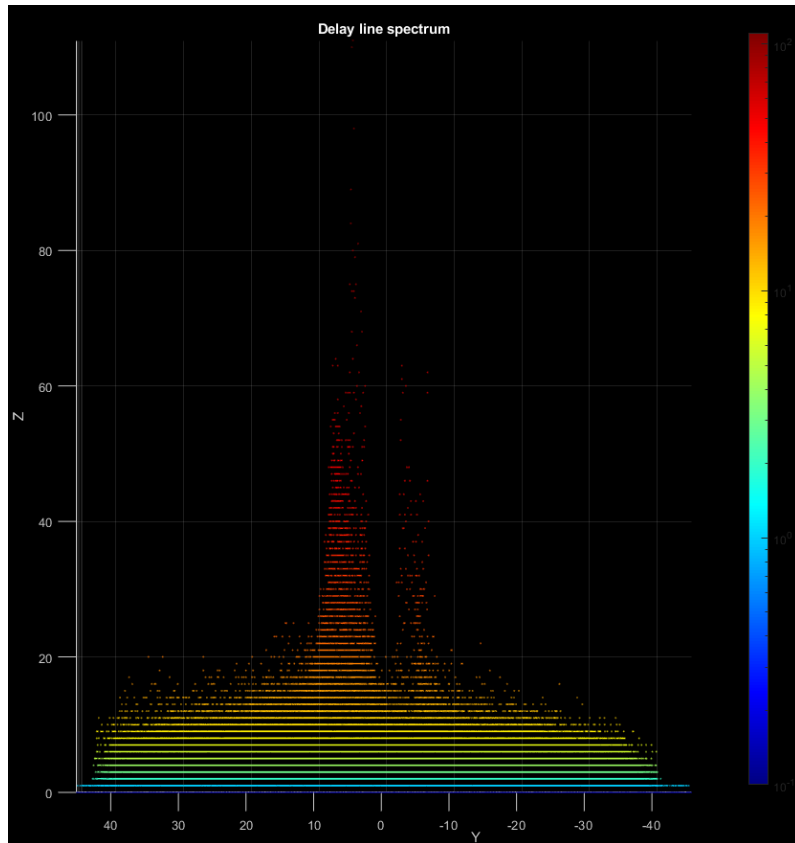
Figure 4.22: Side view of the spectrum produced by the detector during one of the experiments.
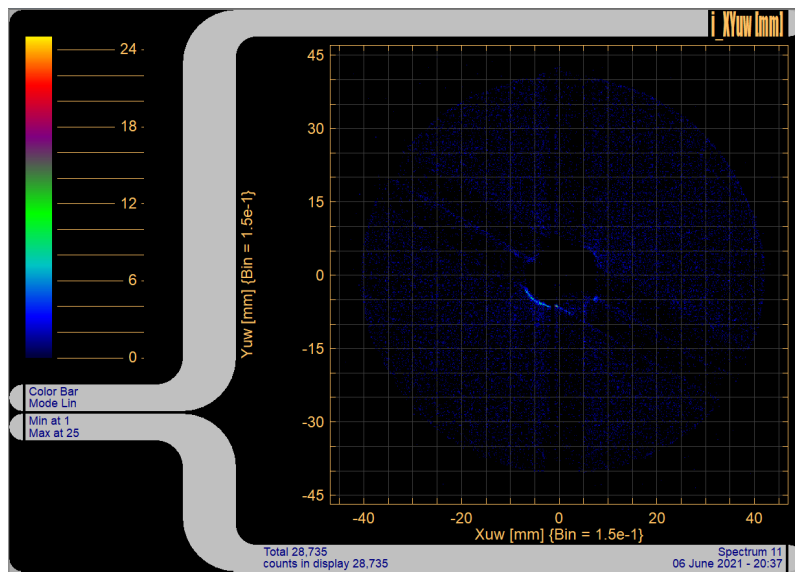

Figure 4.23: The spectrum produced by the delay line detector with the aluminum hollowed shield in front of the MCP stack.

Chapter 5

Conclusions

The aim of this thesis was to:

- presents the general electrostatic model for understanding the generation of the transient voltage perturbations detected by antenna instruments. The matrix form provides a convenient way to track the interaction between the elements and calculate the voltage differences in between. In addition, the elastance matrix offers a straightforward course of calculating the effective capacitances of the elements needed to convert the measured voltages to charge appropriately, or vice versa. Overall, the presented model will improve data analysis fidelity and calculate the impact charge from the dust particle, which in turn allows determining its mass. This is, of course, under the assumption that we know the impact speed, SC potential, and the effective temperatures of the electrons and cations of the impact plasma.It is remarkable how well the model reproduces the measured waveforms, using only a small set of fitting parameters. This fact confirms the suggestions of prior studies that there are two primary signal generation mechanisms: one due to the recollected charge from the impact plasma and the second from the induced charge from the escaping fraction of the impact plasma. One of the fundamentals of the model is the recognition that the collected and induced charges can be treated similarly. If desired, the model can be easily augmented to include the charge collection by the antennas for even higher fidelity. This may be significant for dust impacts occurring in the close vicinity of an antenna base.Shen et al.[2021] presented a simplified model applicable to the simplified case, where the antenna is far from the impact location. The full model presented in this article employs the geometric functions to account for the generation of induced charge signals on the antennas. The measurements have shown that the induced charge is significant even for impacts relatively far from the antenna base. This has several important consequences: (1) The model can be used to analyze the wide variety of expected waveforms from the dust impact signals as a function of impact location (and other parameters, e.g., those of the ambient plasma). Such analysis would be useful for recognizing valid dust impact events. (2) There is a promising outlook that the detailed analysis of the waveforms detected by multiple antennas can be used to constrain the impact location on the SC body, which in turn could provide useful information on the orbital elements of the impacting particle. The induced charge signal from a plasma plume is unique for each antenna and impact location. The small variations between antenna waveforms could thus reveal the origin of dust particles. (3) The previous point can be turned around, and antenna waveforms for a known dust impact location can be used to characterize the properties of dust impact plasma plumes. Our understanding of dust

impact plasmas is surprisingly limited, and antennas may provide an elegant way to learn about the expansion characteristics of the electrons and cations. This method would be applicable both for laboratory measurements and data collected by space missions. (4) It may be worth revisiting the efficiency of dust impact detection for antennas operating in dipole mode. The presented model could be employed to analyze the variety of impact waveforms expected in this mode, which are significantly different from those measured in the monopole mode.

- integrate the the electrostatic model presented with the data obtained during the shooting campaign. The integration process between the electrostatic accelerator and the Three-Layer Delay-Line Anode detector is in the early stages. The three set up proposed for the experiment did not give the angular aperture of the conic expanding plume but showed promising result confirming that ion detection using the detector and the accelerator is possible.(1) The main problem encountered during the experiment in all the three set up proposed were reflections in the y_1 channel as shown in the oscilloscope test. A probable cause for reflections are mismatched impedance caused by cabling. However, the characteristics of all the cables connecting the detector to the feedthrough were the same, yet the problem presented itself only in one single channel. The most probable cause of the reflection was the distance between the connecting pin where the cable was attached to and the aluminum back plate needed to sustain the detector. A new design of the mounting plate might solve the reflection problem. The new design should increase the distance between the back aluminum plate and the pins collecting the delay line signals. Finding a solution to this problem is very important because the spectrum pattern revealed the a dead region area of a two delay line detector. Such region is drastically limiting the capability of detecting multiple hits. In this situation the dead time of the TDC must be taken into and two consecutive hits within Δt_e must be avoided. (2)The detector showed abnormal reading when it was enclosed inside a metallic box. The cause for these abnormal reading was the proximity of the metal box to the MCP frontal plate. The distance between the front of the MCP stack and the aluminum box was set to be 3.5mm, the minimum to avoid electrical discharges. As the metallic box surrounding the detector was removed it was working properly. Hence the shielding of electric fields must be done in alternative ways. The thick aluminum box could be replaced by a fence grid placed at a proper distance from the front plate of the MCP stack. Numerical simulation could reveal the uselessness of shielding static electric fields if the deviation of ions from the original trajectory is negligible or can be corrected by the results of the simulation. (3) Calibration test of the detector showed a noise level caused by causal events of the order of 50 events/s with the used voltage setting. As the fundamental characteristic of the electrostatic accelerator is to accelerate a lower amount of particles with lower masses and higher charges, the number of high speed dust decreases with the increasing of velocity. As it was explained in chapter two the full ionization of the hitting particles occurs at speed higher than 20 km/s. During the shooting campaign the frequency of the particle reaching the vacuum chamber were not enough to surpass the noise level of the detector. Real hit would be lost due to noise. The number of causal events produced by the detector can be reduced, modifying temperature and the voltage settings of the front and back plate. Increasing the voltage difference would cause the increase of causal event per second and decreasing it the gain of the MCP decreases too. Decreasing the temperature inside the chamber could be a valuable solution.

References

[2]H. Dietzel, G. Neukum, and P. Rauser, "Micrometeoroid simulation studies on metal targets", Journal of Geophysical Research **77**, 1375–1395 (1972).

[3]S. Drapatz and K. W. Michel, "Theory of shock-wave ionization upon high-velocity impact of micrometeorites", Z. Naturforsch **29a**, 870–879 (1974).

[4]E. Gr*ü*n, "Calibration of the galilep/ulysses dust detectors with different projectiles ma trials and varying impact angles", ESA Spec. Publ. **224** (1984).

[5]J. R. G*ö*ller and E. Gr*ü*n, "Impact ionization from gold, aluminum and pcb-z", Planet. Space Sci. **37**, 1197–1206 (1989).

[6]N. McBride and J. A. M. McDonnell, "Meteororoid impacts on spacecraft:sporadic, streams, and the 1999 leonids", Planet. Space Sci. **48(8)** (1999).

[7]S. Robertson, Z. Sternovsky, and B. Walch, "Reduction of asymmetry transport in the annular penning trap", Physics of Plasmas **11**, 1753–1756 (2004).

[8]J. R. G*ö*ller, S. Pawlinka, and R. Srama, "Dust accelerator tests with cassini rpws samples", Tech. Rep. **MPIK**, Germany (2007).

[9]A. Collette, E. Grün, D. Malaspina, and Z. Sternovsky, "Micrometeoroid impact charge yield for common spacecraft materials", Journal of Geophysical Research: Space Physics **119**, 6019–6026 (2014).

[10]A. Collette, G. Meyer, D. Malaspina, and Z. Sternovsky, "Laboratory investigation of antenna signals from dust impacts on spacecraft", Journal of Geophysical Research: Space Physics **120**, 5298–5305 (2015).

[11]A. Fletcher, S. Close, and D. Mathias, "Simulating plasma production from hypervelocity impacts", Physics of Plasma **22** (2015).

[12]A. Zaslavsky, "Floating potential perturbations due to micrometeoroid impacts: theory and application to s/waves data", Journal of Geophysical Research: Space Physics **120**, 855–867 (2015).

[13]A. Collette, D. M. Malaspina, and Z. Sternovsky, "Characteristic temperatures of hypervelocity dust impact plasmas", Journal of Geophysical Research: Space Physics **121**, 8182–8187 (2016).

[14]S.-Y. Ye, W. Kurth, G. B. Hospodarsky, T. F. Averkamp, and D. A. Gurnett, "Dust detection in sapce using the monople and dipole electric field antennas", J. Geophys Res. Space Physics **121** (2016).

[15]A. Collette, G. Meyer, D. Malaspina, and Z. Sternovsky, "Interpreting dust impact signals detected by the stereo spacecraft", Journal of Geophysical Research: Space Physics **122**, 11, 864 to 11, 873 (2017).

[16]L.Nouzák, S.Hsu, D.Malaspina, F.M.Thayer, S.-Y.Ye, J.Pavlů, Z.Němeček, J.Šafránková, and Z.Sternovsky, "Laboratory modeling of dust impact detection by the cassini spacecraft", Journal of Geophysical Research: Space Physics, 85–91 (2018).

[17]P. Tarantino, A. Goel, A. Corso, N. Lee, and S. Close, "An electrostatic method to model the expansion of hypervelocity impact plasma on positively biased surfaces", Physics of Plasma **25** (2018).

[18]L. Nouzák, Z. Sternovsky, M. Horányi, S. Hsu, J. Pavlů, M.-H. Shen, and S.-Y. Ye, "Magnetic field effect on antenna signals induced by dust particle impacts", Journal of Geophysical Research: Space Physics **125** (2019).

[19]Kociscak, Å. Fredriksen, M. DeLuca, J. Pavlů, and Z. Sternovsky, "Ieee effective temperatures of olivine dust impact plasmas", Transactions on Plasma Science **48**, 4298–4304 (2020).

[20]M.-H. Shen, Z. Sternovsky, M. Horányi, S. Hsu, and D. Malaspina, "Antenna signals generated by dust impacts on spacecraft", Journal of Geophysical Research: Space Physics (2020).

Books

[1]J. C. Maxwell, *A treatise on electricity and magnetism* (Oxford University Press, 1873).

Appendix A

Capacitance measurements

The measurements procedure explained here were carried out with the Spacecraft model of the satellite inside the vacuum chamber maintaining experimental conditions. The measurement were performed using a voltage function generator and a test capacitor of C_{test}=10pF. The function of the voltage coming out of the generator was a square wave with $\Delta V = 50$mV amplitude. The signal was applied onto the Spacecraft or antennas with the C_{test} in the middle. The charge collected by the conductor was $\Delta V C_{test} = 0.5$pC. As the spacecraft and antennas were collected to the electronics, the voltage response was sent as input into a fast oscilloscope and recorded. The output signals were used to calculate the total capacitance sensed by each system using a SPICE (Simulation Program with Integrated Circuit Emphasis) software tool. The waveform generated by the charge can be seen in the figure below. The same procedure was repeated switching the connection in the spacecraft system in order to reproduce the capacitance matrix and the results were the following
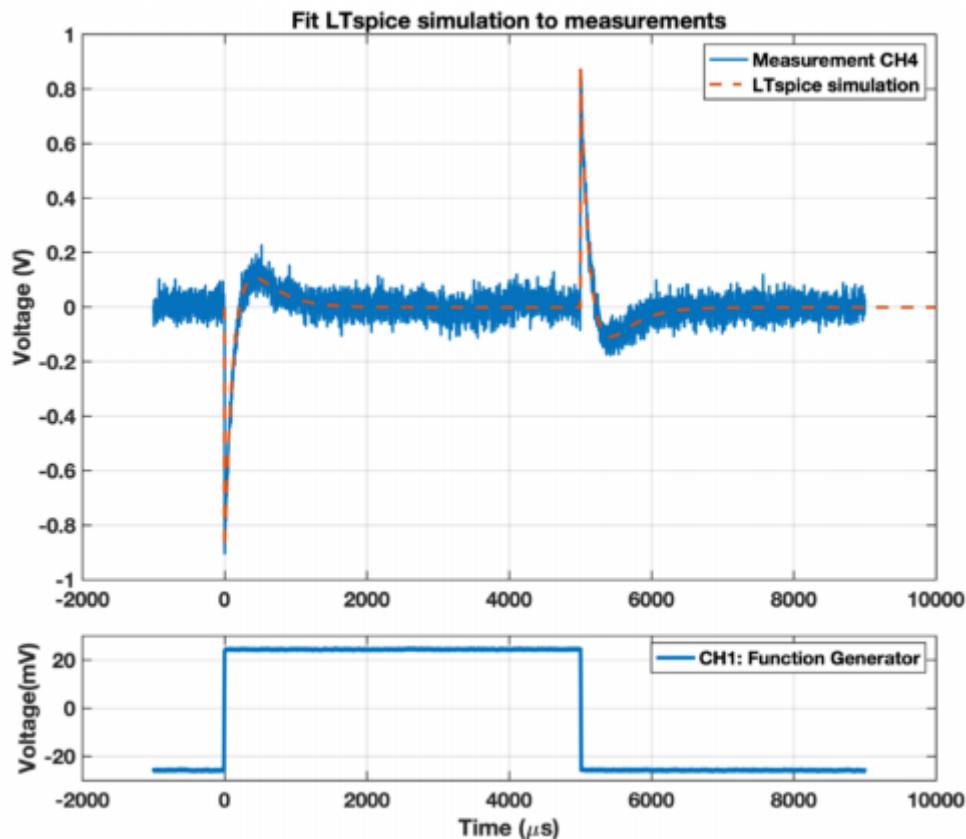

Figure A.1: SPICE simulation of the output voltage signals.

$$SC : C_{test} + C_{SC} + 4C_x \simeq 64pF$$
$$Antenna1 : C_{test} + C_{ANT,1} + C_x \simeq 26pF$$
$$Antenna2 : C_{test} + C_{ANT,2} + C_x \simeq 27pF \qquad (A.1)$$
$$Antenna3 : C_{test} + C_{ANT,3} + C_x \simeq 29pF$$
$$Antenna4 : C_{test} + C_{ANT,4} + C_x \simeq 26.5pF$$

The mutual capacitance were considered to be equal as a simplifying assumption. The capacitance of each elements and the mutual capacitance were the unknowns. As another equation was missing the test charge was sent into one antenna while the other antennas were at ground and the spacecraft potential was left floating. The output voltage for all the measurement were recorded. As final step the Capacitance C_x was left varying in step of 0.5 pF between the value of 4-8 pF. The value of C_x that best fitted all the measurements was 6.5 pF.

Appendix B

Effective capacitance

The RC time constant during the experiment is the combined effect of the resistance connected to the spacecraft and the antennas R = 5 Ω and the effective capacitance C_{eff}. The effective capacitance for each spacecraft antenna system can be computed by means of the capacitance matrix

$$\begin{pmatrix} \delta V_{SC} \\ \delta V_{ANT} \end{pmatrix} = \begin{pmatrix} a_{0,0} & a_{0,1} \\ a_{1,0} & a_{1,1} \end{pmatrix} \begin{pmatrix} \delta Q_{SC} \\ \delta Q_{ANT} \end{pmatrix} \tag{B.1}$$

The charge can be computed as follows

$$\begin{pmatrix} \delta Q_{SC} \\ \delta Q_{ANT} \end{pmatrix} = \begin{pmatrix} b_{0,0} & b_{0,1} \\ b_{1,0} & b_{1,1} \end{pmatrix} \begin{pmatrix} \delta V_{SC} \\ \delta V_{ANT} \end{pmatrix} = \begin{pmatrix} C_{SC} + C_x & -C_x \\ -C_x & C_{ANT} + C_x \end{pmatrix} \begin{pmatrix} \delta V_{SC} \\ \delta V_{ANT} \end{pmatrix} \tag{B.2}$$

where $b_{i,j} = a_{i,j}^{-1}$. Performing the multiplications in the previous equation the charge perturbations reads

$$\delta Q_{SC} = (b_{0,0} + b_{0,1})\delta V_{SC} + b_{0,1}(\delta V_{ANT} - \delta V_{SC})$$
$$\delta Q_{ANT} = b_{1,0}(\delta V_{SC} - \delta V_{ANT}) + (b_{1,1} + b_{1,0})\delta V_{ANT} \tag{B.3}$$

Where the difference of potentials between the spacecraft and antenna are introduced. By means of substitution

$$\delta Q_{SC} = C_{SC}\delta V_{SC} + C_x(\delta V_{SC} - \delta V_{ANT})$$
$$\delta Q_{ANT} = C_x(\delta V_{ANT} - \delta V_{SC}) + C_{ANT}\delta V_{ANT} \tag{B.4}$$

The derived set of equation can be solved either for the spacecraft collection case or the antenna collection. As during the experiment the spacecraft body dust hits were simulated $Q_{ANT} = 0$. As $V_{ANT} = V_{SC}C_x/(C_x + C_{ANT})$ the charge variation on the spacecraft reads

$$\delta Q_{SC} = C_{SC}\delta V_{SC} + C_x(\delta V_{SC} - \frac{C_x}{C_x + C_{ANT}}\delta V_{SC}) \tag{B.5}$$

The obtained equation allows the computation of the effective capacitance as follows

$$\frac{\delta Q_{SC}}{\delta V_{SC}} = C_{eff,SC} = C_{SC} + \frac{C_x C_{ANT}}{C_x + C_{ANT}} \tag{B.6}$$

Hence the time constant discharging time is $\tau = C_{eff,SC}R_{Bias}$